Stony Brook University

Tomographic Analysis and Simulation of Reactive Flow in Column Experiments.

A Dissertation Presented

by

Rong Cai

to

The Graduate School

in Partial Fulfillment of the

Requirements

for the Degree of

Doctor of Philosophy

in

Applied Mathematics and Statistics

Stony Brook University

December 2009

Stony Brook University

The Graduate School

Rong Cai

We, the dissertation committee for the above candidate for the degree of Doctor of Philosophy, hereby recommend acceptance of this dissertation.

W. Brent Lindquist
Professor of Department of Applied Mathematics and Statistics
Dissertation Advisor

XiaoLin Li
Professor Department of Applied Mathematics and Statistics
Chairman of Defense

Xiangmin Jiao
Professor of Department of Applied Mathematics and Statistics
Committee Member

Keith Jones
Adjunct Professor of Department of Material Science and Engineering
Outside Member

This dissertation is accepted by the Graduate School.

Lawrence Martin
Dean of the Graduate School

Abstract of the Dissertation

Tomographic Analysis and Simulation of Reactive Flow in Column Experiments.

by

Rong Cai

Doctor of Philosophy

in

Applied Mathematics and Statistics

Stony Brook University

2009

Adviser W. Brent Lindquist

Dissolution followed by precipitation is a major mechanism in the formation of secondary precipitates in most porous sediments. Secondary precipitation is of interest as a structure modifying mechanism that may also control contaminant transport in the subsurface environment. Quantification of structural change is a necessary component for the construction of predictive models for effective reaction rates at field scales.

We have employed synchrotron X-ray computed microtomography in combination with flow-column experiments to capture and quantify snapshots in time of dissolution and secondary precipitation changes in the microstructure of Hanford sediments exposed to simulated caustic waste in flow-column experiments. Careful image analysis was done to address the anticipated systematic errors. Changes accompanying a net reduction in porosity of 4% were quantified including:(1) a 25% net decrease in pores resulting from a 38% loss in the number of pores $< 10^{-4}$ mm^3 in volume and a 13% increase in the number of pores of larger size; and (2) a 38% decrease in the number of throats. The loss of throats resulted in decreased coordination number from pores of all sizes

and significant reduction in the number of pore pathways.

A reactive flow network model was developed to simulate the evolution of the chemical species resulting from the reactions in a flow-column experiment and under batch experiment conditions. This single network flow modal incorporated both kinetic (for dissolution and precipitation of solids) and instantaneous (for equilibrium of aqueous species) reactions, as well as advection and diffusion of concentrations in the pore space. The single phase flow model incorporated channel conductances based upon more exact, pre-computed, Lattice-Boltzmann computations. The reactive network flow simulation indicates that, after initial quartz dissolution, secondary precipitation dominates in the pore space within six hours of initialization of flow resulting in eventual equilibrium of silicon ion concentration, [Si], (from quartz dissolution) and aluminum ion concentration, [Al], (carried in the invading solution). After halting further fluid input (to simulate batch reactor conditions), dissolution begins to dominate again, resulting in increased [Si] and decreased [Al].

Table of Contents

List of Tables

List of Figures

Chapter 1

Introduction

Dissolution and precipitation are primary reactions in mineral formation and weathering in the geosphere, playing critical roles in natural processes (diagenesis, chemical weathering, hydrate dissolution/formation) and in engineered processes (simulation of petroleum reservoirs, contaminant sequestration/mobility, bioremediation). Precipitation accompanying dissolution is a major reaction mechanism in forming secondary precipitates in most porous sediments, the precipitates existing as surface coatings or cementing materials between mineral grains. Such secondary precipitation is of interest as it can modify pore structure and control the transport of anthropogenic waste in the subsurface environment [1, 22, 61].

This thesis is ultimately motivated by the fact that uranium has been observed to be retained as uranium-silicate secondary precipitates in feldspar micro-fractures and granite clasts of vadose zone sediments after contact with leaking caustic tank waste solution at the legacy US Department of Energy (DOE) Hanford site in southern Washington State [2, 39, 67, 65], Washington. To understand the reaction chemistry, there have been a number of laboratory batch and flow-column experiments performed on model and actual Hanford sediments [7, 14, 15, 30, 50, 51, 54, 62], which predominantly consist of quartz

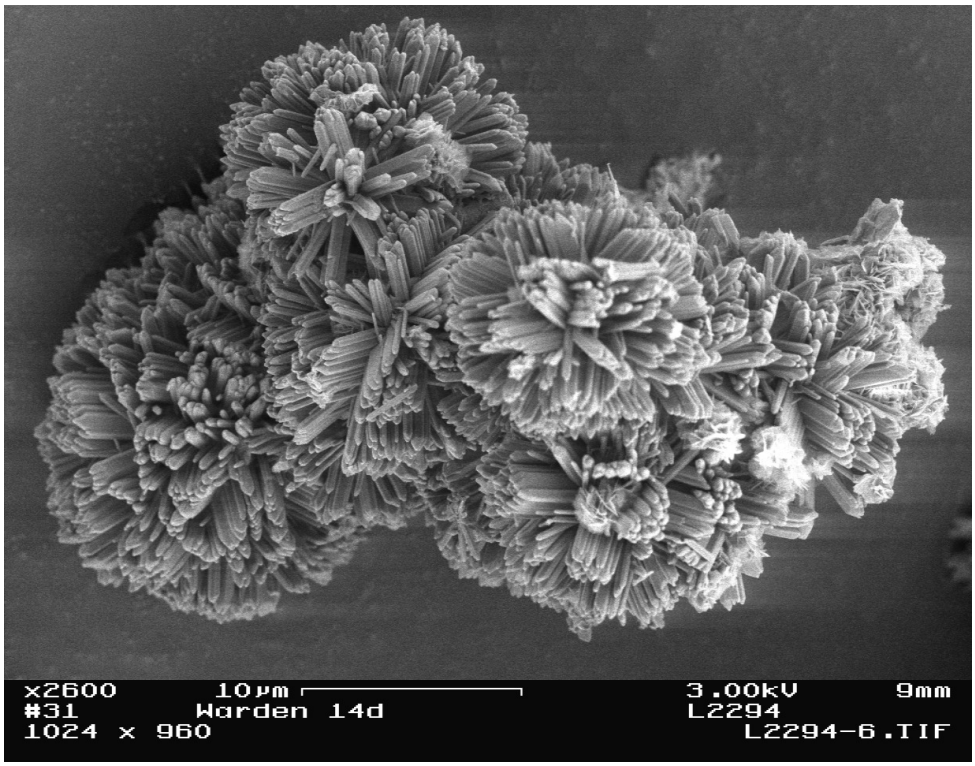

Figure 1: CMT image of cancrinite precipitants on Wardan soil sample after 14 days exposure to the reactive flow at a resolution of 10 μm. Image provided by Dr. Wooyang Um, PNNL.

grains, and on related high alkalinity systems [3]. These experiments have demonstrated that simulated caustic tank waste leachates dissolve this primary mineral, resulting in the continuous release of Si to the pore water solution and a dominant secondary precipitation of sodalite and cancrinite [7, 14, 15, 30, 50, 62] (Fig. 1), which nucleate on the cement together quartz grains. Both Cs and Sr have been observed to be incorporated into these secondary feldspathoid minerals. Caustic wastes that have leaked at the Hanford site can therefore induce mineral dissolution and subsequent secondary precipitation with the potential to influence the fate and transport of the radionuclides present in the waste [9, 10].

We have employed high resolution (4 μm voxel size), synchrotron CMT,

combined with a flow-column experiment involving surrogate caustic waste solution and Hanford soil. The goals of this research work are to:

1. document the accompany structural changes and to identify the preferential areas, if any, in the network of the dissolution and secondary precipitation at conditions that approach field parameters. Quantification of these changes is a necessary component for the construction of predictive scale up models for effective reaction rates at field scales;

2. simulate the concentration evolution of the reactive species in order to predict reaction changes at the pore-scale using a single phase reactive network flow model.

1.1 Review of Previous Studies on Reactive Flow

Kang at al. [26] provide a succinct, introductory review (through 2003) of experimental and computational studies of structural changes accompanying dissolution and precipitation in geologic media. A major focus has been on dissolution, initially to optimize wormholing (channeling) as a technique for oil reservoir recovery stimulation via acid injection. Experiments have targeted dissolution in the bulk matrix and fractures [12, 21, 23, 16, 17, 19] of predominantly single mineral media. Experimental techniques have included Wood's metal casts [12, 23], neutron radiography of Wood's metal casts [21], NMR [17, 18], light transmission [16] and profilometry [19]. The experimental work has been augmented by theoretical analyses in simple geometries (e.g. [11]) and computational studies [5, 6, 25, 29, 28, 59, 60]. Recently, there has been intense interest in lattice Boltzmann based models [25, 29]. Except for idealized geometries, the computations have largely been two dimensional. Experimental techniques based upon Wood's metal casts are destructive to

the sample. Profilometry and light transmission are restricted to thin section studies. NMR spatial resolution ($\sim 10^{-1}$) is relatively coarse.

Beginning in 2001, studies have emerged on secondary precipitation in Hanford soils resulting from exposure to simulated Hanford tank solutions. The experiments have included using scanning electron microscopy (SEM) [7, 64] and X-ray microtomography [64] in both batch and column experiments. The SEM studies have revealed the existence of etching pits and secondary precipitate growth on the surface of individual grains resulting from hyperalkaline flows. SEM operates on nanometer length scales and is able to capture the precipitate crystallinity morphology. However, nanometer resolution is too fine to obtain global perspectives on spatial changes. At much larger scales (40 μm voxel size), Um and Serne [64] employed X-ray tomography (CMT) to image (before and after) model Hanford soil columns exposed to reactive caustic solutions to investigate the potential pure structure modifications induced by dissolution and secondary precipitation. The experiments observed the changes of flow path from an evenly distributed flow throughout the whole cross-section of the inlet portion of column to a preferential flow mainly along the edges of the column farther from the inlet, which suggested that dissolution occurred from the flow inlet and precipitated at the center of the middle of the column increasing cementing processes that led to changes in flow paths. Due to the resolution limitation in their CMT system, their results could be used only for qualitative interpretations on the effects of mineral dissolution and secondary precipitation on changes in pore structure and fluid flow properties.

1.2 Flow-Column Experiment and CMT Imaging

We have repeated the work of Um and Serne [64] to demonstrate that X-ray computed micro-tomography (CMT) at finer resolution can be used to capture and quantify the micro-structural changes taking place during the reactive flows. For such studies, CMT imaging requires a resolution balance - resolution must be sufficiently fine to capture changes at the level of individual pores yet the region imaged must be large enough to canvas a meaningful sample of pores. Using the X2B beam line facility at the National Synchrotron Light Source (NSLS) at Brookhaven National Lab (BNL) [13, 20], we obtained images with a voxel size of 4 μm. Details of the flow-column experiment design and CMT imaging process are described in Section 2.1 and 2.2.

In addition to the increased image resolution, we have introduced two other advances/changes over the work of Um et al. First, we utilized the non-destructive nature of CMT to obtain a time sequence of images in order to document temporal changes. The column was imaged on five separate occasions - after initially flooding with groundwater, and after each of four separate periods of flooding with the caustic solution. Second, the higher voxel resolution necessitated a thinner diameter column, we therefore scanned several sections along the length of the column to capture a larger reactive volume.

One factor complicating the results is the periods, sometimes lengthy, of time during which the column was sealed and awaiting imaging. During these periods of time, the column acted like a batch reactor rather than a flow column. The results obtained are therefore a combination of effects obtained from a "flow column" - "batch reactor" sequence.

Even with 4 μm resolution, we were working close to resolution limits for observing structural changes in this reactive system. The most critical need

in the analysis was to determine whether the observed structural changes captured any trend, and whether the trend was real or was masked by possible systematic errors. Therefore, the analysis has been careful to address anticipated systematics. In Section 2.3 we describe the analysis of the experiment images.

In Chapter 3 the microstructure changes in the pore space are quantified, and compared with the detection of the porosity changes from the segmented data and effluent concentration evolution that was measured from the experiments.

1.3 Reactive Network Flow Model

In Chapter 4 we introduce preliminary studies performed using a reactive network flow model. The reactive model incorporates advection of the reactive fluid, chemical reactions in the pore space as well as on the grain surfaces, and diffusion of aqueous chemical species among the neighboring pores.

In Section 4.1 the design of reactive model is explained and initial and boundary conditions defined. The single phase network flow is introduced to calculate the fluid advection. The detailed explanation of how diffusion and reactions are modeled follows. We describe the kinetics of dissolution and precipitation of surface minerals. These two reactions are the most important factors for the evolution of chemical species inside the column. However, the aqueous chemical species that are produced from these two kinetic reactions are not stable in the fluid. Instead, they react with water instantly and form acid or alkaline ions. These aqueous reactions are fast; the final concentration of these species and their new products follow specific equilibrium relationships. Our model takes these equilibrium reactions into consideration.

In Section 4.3 we supplement the channel conductance computation that

is used in the flow computation. Instead of using traditional shape factor models for channel conductance [42, 44], Lattice-Boltzman (LB) computation was used to capture the local geometry of throat channel. In Section 4.3, we present the LB computation based power fit model [56] to predict the throat channel conductance. The LB computation results revealed a power fit relationship between throat shape factor and throat conductance. We applied the power law fit to the conductance computed for four sections of the column. We show that our LB computation based power law fit provides a much better estimation of throat channel conductance than the traditional shape factor model.

The reactive model was implemented and used to simulate the Hanford reactive flow-column experiment. The simulation was done following a "flow-column" - "batch reactor" sequence using one section of the column data from the CMT imaging. The results of this preliminary study is shown in Section 4.5 with discussion in Section 4.6.

Chapter 2

Materials and Methods

2.1 Flow-Column Experiment

The uncontaminated Hanford sediment (C2177-110) used in the columns was collected from borehole C3177 (well 299-E24-21) in the 200 East Area of the Hanford Site. The sediment, representative of Hanford coarse sand, consisted of a mixture of gravel (3.9 wt%), sand (89 wt%), silt (6.2 wt%), and clay (1.4 wt%). A narrow range of grain-size fraction (212-300 μm in diameter) screened from the sediment was used for the column experiments. Uncontaminated Hanford groundwater (pH 7.5) collected from well 699-S3-25 at the Hanford site was used as initial background solution in the column experiments. Additional details on the sediment and groundwater compositions can be found in [63] and [64]. Simulated tank leachate was prepared using reagent grade chemicals and consisted of 1 M $NaNO_3$, 1.2 M NaOH, and 0.05 M $Al(NO_3)_3$. This choice, which is towards the lower end of the total ionic-strength range for bulk tank compositions, was based upon two factors. The first is that caustic solutions at the upper end of the ionic-strength range (12 M) are very difficult to handle experimentally. The second is that dilution of the ionic-strength of the waste solution is to be expected during movement

through the subsurface.

The flow-column experiment runs were conducted by Wooyong Um in Pacific Northwest National Laboratory (PNNL) using a poly-etherether-ketone (PEEK) column of height 8.8 cm and inner diameter 3.1 mm. The small diameter was dictated by a combination of imaging considerations: the 4 μm voxel size, reasonable imaging times, and beam energy. The total interior volume of the column was 0.66 cm^3; total mass of sediment filling the column was 1.0 g. The ends of the column were covered by 5 μm Spectra/Mesh to retain particles. The column was packed using a continuous particle stream while vibrating the column on a Vortex-Genie 2 mixer (Fisher Scientific) to achieve uniform packing. The column was initially saturated with uncontaminated Hanford groundwater that was allowed to flow through for at least 2 days at room temperature to stabilize the flow and remove easily dispersible particles. A constant upward flow rate of 0.67 ml/day (approximately 1 PV/day) was maintained during this saturation period using a peristaltic pump to minimize depositional effects due to gravity and to ascertain complete saturation. Fig. 2 is a picture of the flow column experiment set-up at PNNL. Due to the very low X-ray attenuation of air, the presence of gas bubbles in the interior of the sample can easily be detected under CMT. None were so observed in the sections of the column that were imaged indicating that saturated conditions were achieved and maintained in the column throughout the experiment.

After flow stabilization, the column was sealed by closing the end cap valves and shipped to Brookhaven National Laboratory (BNL) for initial tomography imaging at the National Synchrotron Light Source (NSLS). At BNL, a piece of lead foil tape, approximately 2.5 mm wide, was wrapped around the column, 3.1 cm from one end. The inside edge of the tape (i.e. 3.35 cm from the end) was used for alignment of CMT imaging, and for alignment of flow direction during subsequent column flooding. Fig. 3 presents a schematic of the column

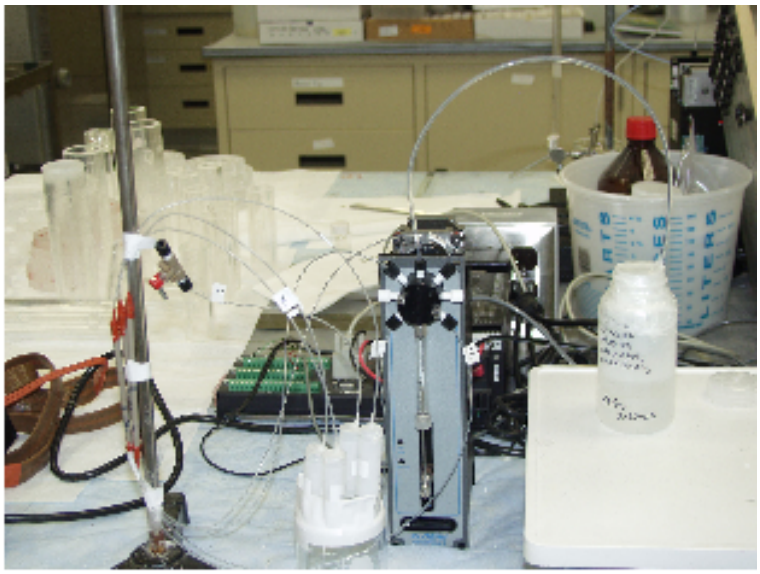

Figure 2: Set up of the column flow experiment in PNNL.

flow experiment showing the orientation of the column during flooding and CMT imaging. Note that the column is rotated 180° vertically between flow experiments and imaging - this has the effect that the "top" of any image taken on the column is toward the inlet end where the fluid enters.

After the initial scan of the unreacted column, it was returned to PNNL for a series of exposures to the synthetic caustic leachate. The leachate was introduced into the column with the same pump setting as used for groundwater. The effluent was collected periodically for analysis of major cations (Si, Al, and Na) using inductively coupled plasma optical emission spectroscopy (ICP-OES). Table 1 summarizes the reactive floods performed on this column. Fig. 3 summarizes measured effluent concentrations. At the termination of each run, the column was re-sealed and shipped to BNL for imaging. All the experiments were done at room temperature (25 $^{\circ}C$).

Pump settings were held constant and eluted volumes were observed for each run enabling the computation of average and standard deviation flow rates. The flow rate through the core was observed to fall from an initial rate

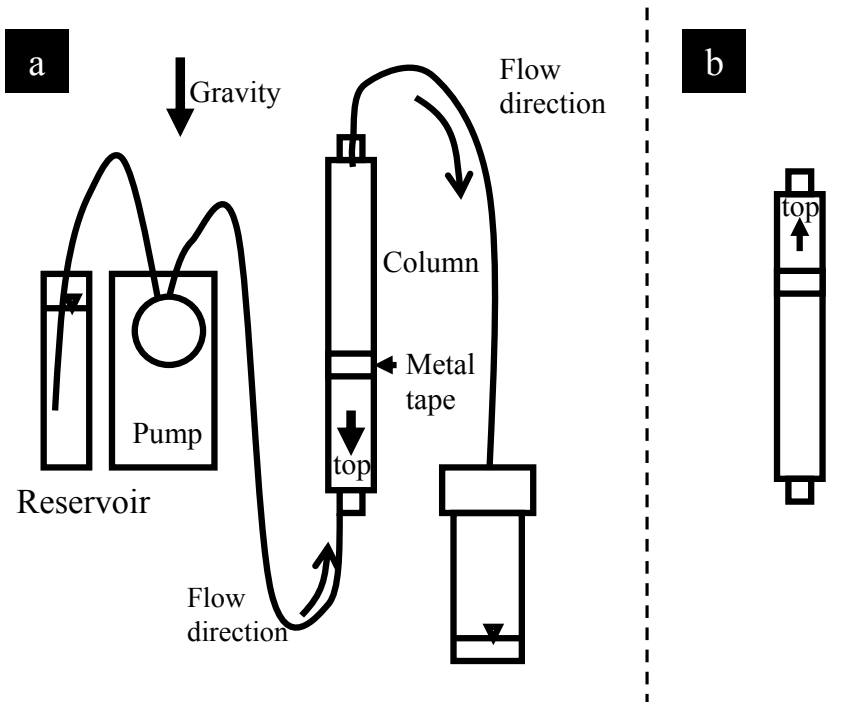

Figure 3: (left) Schematic of column flow experiments. (right) Orientation of column during CMT scans.

of 0.67 ml/day for saturation flow with uncontaminated ground water to 0.238 ± 0.179 ml/day in after 106 days of flow exposure to caustic solution.

Run	0	1	2	3	4
Start time		16:00 5/12/06	10:50 9/20/06	15:15 2/9/07	15:15 9/15/07
End time		13:10 6/27/06	16:25 10/13/06	10:10 2/26/07	16:00 10/05/07
Duration, days	2	46	23	17	20
Solution	ground water	STM	STM	STM plus 10^{-3}M $Sr(NO_3)_2$	as in run 3
Rate, ml/day av (std dev)	0.67	0.553 (0.139)	0.33 (0.001)	0.301 (0.007)	0.238 (1.179)
Voxel size (μm)	3.97	3.94	3.97	3.97	3.97
Energy (keV)	20.005	25.000	22.000	21.998	22.000

STM – Simulated tank reactant: 3 M Na^{+*},1 M OH^-,1.15 M NO_3^-,0.01 M $Al(OH)_4^{-*}$
* As determined by ICP-OES measurement on the simulated tank waste solution.

Table 1: Flow specifics for the column experiment and main CMT parameters.

2.2 X-Ray Computed Tomography (CMT)

After initial stabilization (saturated flow with uncontaminated Hanford ground water) and subsequent to each flood by tank stimulant, the sealed columns were imaged using the CMT scanner on bean line X2B [13, 20] at the NSLS facility at BNL. The scanner was used with the silicon (111) single-crystal monochromator in place to provide a narrow bandwidth (±20 eV) of X-ray photon energy. Mean X-ray energies used for each image are also given in Table 1.

The X2B specimen-mount stage consists of: a manual axis-pitch stage; computer-controlled, motorized, precision x-, y- and z-translation and rotation stages; and a four-axis manual goniometer into which the specimen is

typically mounted. The mounting stage provides specimen alignment, region-of-interest selection, rotation, horizontal translation (to pull the specimen from the field of view for calibration) and vertical translation (to schedule multiple vertical region-of-interest scans). Due to the height of the column, the manual goniometer was swapped for a (short height) three-jawed chuck. This replacement reduces the ability to align the center of rotation with the center of the column. However this loss is not critical as long as the entire width of the sample remains within the field of view during a 180° rotation. The sample was rotated at 0.15° increments, producing 1200 projections.

The imaging stage consists of a thallium-doped cesium iodide crystal (0.5 mm thick) to convert the X-ray image into a light image. The light image was projected with a microscopy objective lens (5X) onto a charge coupled device (CCD) imaging array consisting of 1340×1340 square pixels, each pixel being 20 μm on a side. Use of the 5X lens produces effective voxel sizes of about 4 μm on a side. The exact voxel sizes obtained, as determined from voxel counting across known distances on the sample projections, are given in Table 1. The projection images were digitized at 16-bits. Full readout of the CCD array over 1200 projections at 16 bit accuracy produces files of size 4 GBytes. However, readout from a specific area of the CCD camera is possible; to keep projection image file sizes around 2 GBytes, only the central 600 or 800 rows of the CCD array were retained for reconstruction.

After each 60 angle-projections, the specimen was withdrawn from the field of view and white-beam (raw beam, no sample) and black-beam (no-beam, no sample) images taken. These are used to correct the specimen projections for beam, scintillator and CCD non-uniformities. In addition to these standard corrections, each projection was acquired in two separate, equal-time-interval segments, with a 10 μm horizontal (perpendicular to the beam) translation of

the sample made between data collection over the two time segments. Subtraction of the two image intensities thus was obtained for identical specimen point, which allows for the identification and subtraction of intensity features that do not translate with the specimen.

Image reconstruction from projections was performed using the IDL-based software package developed by GSECARS [53] . The package uses the standard Fast Fourier Transform reconstruction technique. It was modified to take, as input, the format of the projection files produced at X2B.

The lower edge of the lead foil tape wrapped around the column was used as a rough fiducial marker to align image taking. Starting with the lower edge of the tape visible in a projection, a sequence of 4 vertical, overlapped images were taken by raising the sample a precise distance after each image. The precise sequences of images scanned over all 5 runs are summarized in Fig. 4. In run 0 each image had 1300 reconstructed slices; in runs 1 and 2, 800 slices; and in runs 3 and 4, 600 slices. The data file for one scan (99-3) from run 2 is missing. In the figure, each scan is represented as a labeled, vertical line. Top sections of the reconstructions of 57-1, 7403, 21-2 were unusable. Two scans, 75-1 and 75-2 are completely unusable due to unexpected beam dumps that occurred during the course of the scan, producing too few projections for viable reconstruction. The symbolic "columns" (rectangles) in Fig. 4 indicate the total composite image that could, in principle, be constructed using appropriate segments from each image. Thus for run 0, a reconstructed length of 2863 slices (11.39 mm) is possible.

Fig. 5 illustrates a typical projection and sinogram (a stack composed of the same slices viewed at all 1200 angles). Each scan was reconstructed, and stored, separately. As each projection is 1340 voxels wide, reconstructed slices have size 1340×1340. However the cylindrical soil column centered in each slice had a diameter of approximately 780 voxels. Thus only a square area

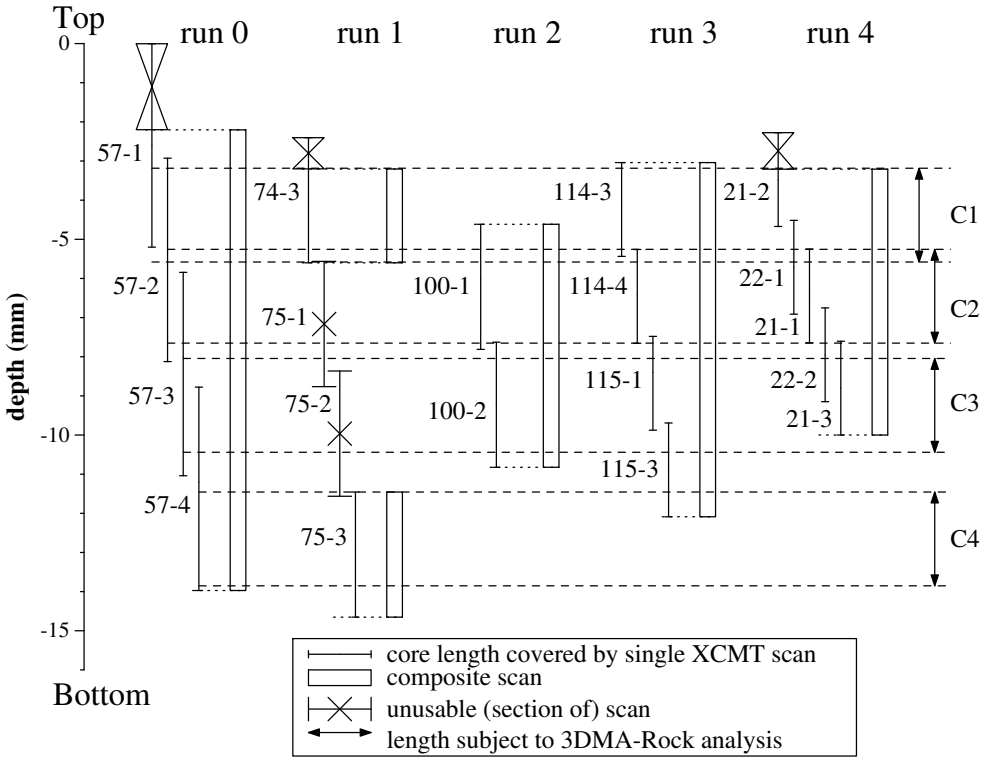

Figure 4: Summary of scans taken and 3DMA-Rock analysis performed on the column. C1 → C4, of the column were analyzed.

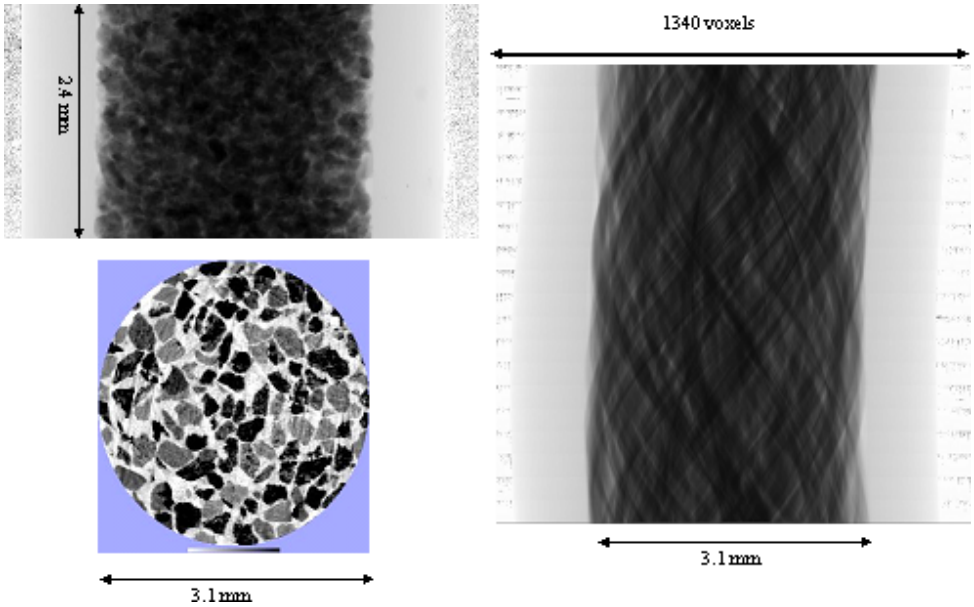

Figure 5: (top left) Projection view for the 600 slice sub-volume (C2) analyzed from image 57-2. (right) Sinogram for the slices in the middle of this sub-volume. (bottom left) Central portion of the reconstruction of this slice.

enclosing the column in each reconstructed slice was retained for analysis (e.g. Fig. 5 - bottom left).

2.3 3DMA-Rock Software Package

In this work, four image sections of the column, labeled C1 through C4 (see Fig. 4 for registration), each of volume 17.9 mm^3, covering a total of 1.2 cm length of the column (from 3.4 cm through 4.6 cm from the inlet end), were extensively analyzed. All the images were analyzed using the 3DMA-Rock software package [31]. 3DMA-Rock is a numerical package developed by W. Brent Lindquist to analyze the pore space in three- (and two-) dimensional X-ray computed microtomographic (XCMT) images of rock. The main algorithms are described in [32].

Fig. 6 succinctly describes the algorithm flow used in 3DMA-Rock package.

The image analysis algorithms for the pore space consist of five general steps:

1. image segmentation, converting the grey-scale tomography image that records the CT value for each voxel (with value from 0 to 2^{16}-1) into a two-phase (grain/void) space;

2. extraction and modification of the medial axis of the pore space, a two-dimensional description of the three-dimensional domain, which preserves the geometric characteristics of the void space as well as provides a powerful search tool for further throat finding and pore-throat network construction;

3. throat construction, using the medial axis as a search path to locate the minimum cross section area that connects the neighboring pores;

4. pore surface construction via marching cubes, providing the surface area (reaction area) for network reaction modeling;

5. assembly and geometrical characterization of the pore-throat network [34, 33, 47, 48, 55], quantifying the important micro-scale properties.of the porous media, including channel conductance, absolute/relative permeability, etc..

These steps are discussed in the following sections as applied to the reactive-flow column images.

2.4 Image Analysis

As seen from Fig. 4, reconstruction of a composite image by appropriately eliminating overlap regions between successive vertical images is possible for all runs except run 1. However, to guard against introduction of systematic errors, as well as for memory-usage reasons (a fully reconstructed 4-Byte image for run 0 which consists of 2863 slices with slice sizes 8000×8000 voxels would require 7.4 GBytes to store and at least double that memory to process), analysis of - and comparison between - runs was done on sampled sections taken from

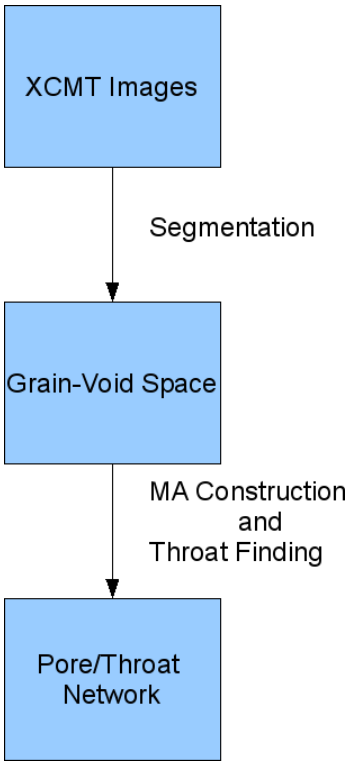

Figure 6: Schematic of 3DMA-Rock software package.

individual images whenever possible. Therefore four sections, C1 → C4, of the column were analyzed (Table 2 and Fig. 4). By way of explanation of Fig. 4: the 600 slice section labeled C1 was analyzed in run 0 (using slices from images 57-1 and 57-2), run 1 (image 74-3), run 3 (image 114-3) and run 4 (slices from images 21-1 and 22-1). From Fig. 4, it can be seen that no full 600 slice image of region C1 was available for run 2 (due to the missing data set 99-3). The four sections, C1-C4 were chosen to increase sampling statistics, and to examine the column along its length.

Label	# slices	images used
C1	600	57-1,57-2;74-3;114-3;114-4;21-2;22-1
C2	600	57-2;100-1;114-4;21-1,22-2
C3	600	57-3;100-2
C4	600	57-4;75-3

Table 2: Summary of analyzed sections.

In order to determine whether observed microstructure changes captured any trend, our analysis has been careful to address anticipated systematics. We have :

1) compensated for the change in voxel size over the 4 runs by adjusting the diameter of the region of interest(ROI) accordingly;

2) rotated the sections axially to give all samples the same digitized orientation, minimizing possible direction dependent systematics in the 3DMA-Rock algorithms used to analyze the data;

3) vertically aligned the different runs to ensure that the same vertical range is compared over time (within a resolution of 1-2 voxels);

4) compensated for the change in illuminating X-ray energy by linearly mapping the segmentation parameters, T_0 and T_1, accordingly;

5) wherever possible, used regions from a single, simultaneously collected stack to avoid any variation of experimental parameters between images. There are two exceptions to this, both in section C1.

   (a) In run 0, image 57-2 is the only image stack that covered the whole 600 slices in C1 section. However, analysis of the attenuation coefficient distribution versus depth (slice number) revealed a discrepancy between the top slices and the rest. The average intensity of the CT values vs slice for C1 sections in both image stacks 57-1 and 57-2 are plotted in Fig. 7. Slices 65 - 664 are the 600 slices that should have been used as the correctly aligned section for C1 at run 0. However, Fig. 7 shows that the average intensity of the CT values of each slice in the images are inconsistent with depth. For the first 287 slices, the intensity range is increasing with the depth, which could be resulted from a change in the X-ray energy in the imaging process. This discrepancy was addressed by using slices 797 - 1083 data from 57-1 to substitute slice 65-300 from 57-2 (Fig. 4). As can be seen in Fig. 7, the slice intensity range of CT values in 57-1 is consistent between slices and is consistent with that of slices 301-600 from 57-2.

   (b) In run 4, no single image covered the section C1 and appropriate non-overlapping slices from 21-2 and 22-1 were used;

6) analyzed four sections (labeled C1 through C4) of the column, each 600 slices in height (volume of 17.9 mm^3), covering approximately 1.2 cm of total imaged length (Fig. 4). Prior analyses [33] on Fontainebleau sandstones, have shown this to be a volume size that generates reproducible statistics on the pore network (i.e. is a REV). We note that Fontainebleau sandstone provides a not unreasonable comparison in that

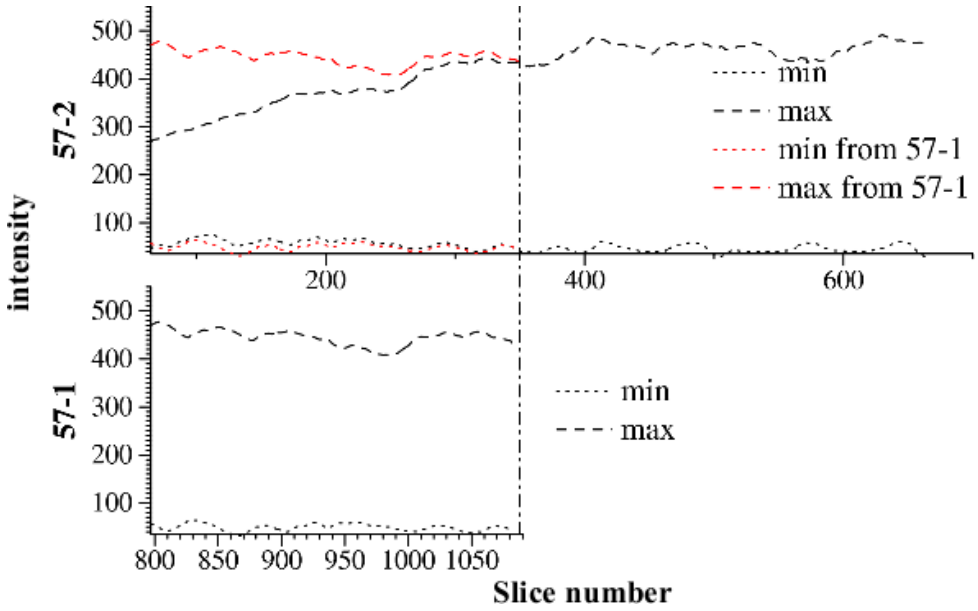

Figure 7: Intensity plot of CT values for single slices versus the depth for 57-1 and 57-2. 57-2 is the only data in Run 0 that cover the C1 section. (First plot from top)Intensity plot of CT values of 600 slices in 57-2 that aligns with C1 section. The vertical line at the depth of 900 microns (300th slice) indicated the location of the last slices of the stack that showed the discrepancy in the intensity. (Second plot from top) Intensity plot of the CT values for the problematic slices. (Third plot from top) Intensity plot of the CT values of slice 301-600 that were consistent and have been preserved in the C1 section for Run 0. (Bottom plot) The intensity plot of all the slices from 57-1, which showed a consistent intensity among all the slices and with the "healthy" slices from 57-2.

> it is a well sorted rock, with grain sizes narrowly distributed around 250 μm - and therefore well matched both in grain and pore size with the sediment sample used here.

We use section C2 to explicitly illustrate the discussion of the procedures 1)$\rightarrow$ 6) above by doing the image segmentation and registration properly.

2.4.1 Image segmentation

Table 1 records two discrepancies in the CMT parameters used to obtain the images in sequence, namely the (slight) difference in voxel size and illumination energy changes among the runs. Both the changes in voxel size and X-ray energy have the potential to introduce systematic errors into the analysis.

Fig. 8 illustrates the problem with changing X-ray energy. The middle plot compares the distribution of CT values for image 57-2 (red trace with two peaks) with the distribution for image 100-1 (green trace with two peaks). The lack of alignment of the peak positions is directly attributable to the change in illumination energy of the X-rays. (Higher energy X-rays give smaller CT values for any given material.) Segmentation (identification of grain and void voxels) of any image by the method of indicator kriging used in the 3DMA-Rock software requires setting two CT values, T_0 and T_1, which define a window. Given the window, the algorithm defines the voxels with CT values below T_0 as void space, those above T_1 as grain phase. Voxels with CT values lying between T_0 and T_1 are phase identified using an indicator kriging algorithm [41], which gives a maximum likelihood prediction of the phase type. If the imaging processes were exactly the same for different runs, the same pair of T_0 and T_1 values should have been used consistently for all images to avoid systematic errors. However, a change in illumination energy results in the shift of the CT value distribution, thus necessitating a change in values for T_0 and T_1. In order to eliminate potential user-bias in selecting T values, T values used for 100-1 were scaled from values used for 57-2 as follows.

As noted, the CT value distribution for each image consists of two significant peaks (corresponding, left to right, to void and grain phases) and an interpeak minimum. We assume that the CT value of both grain and void voxels is distributed normally with different mean (according to the two peaks

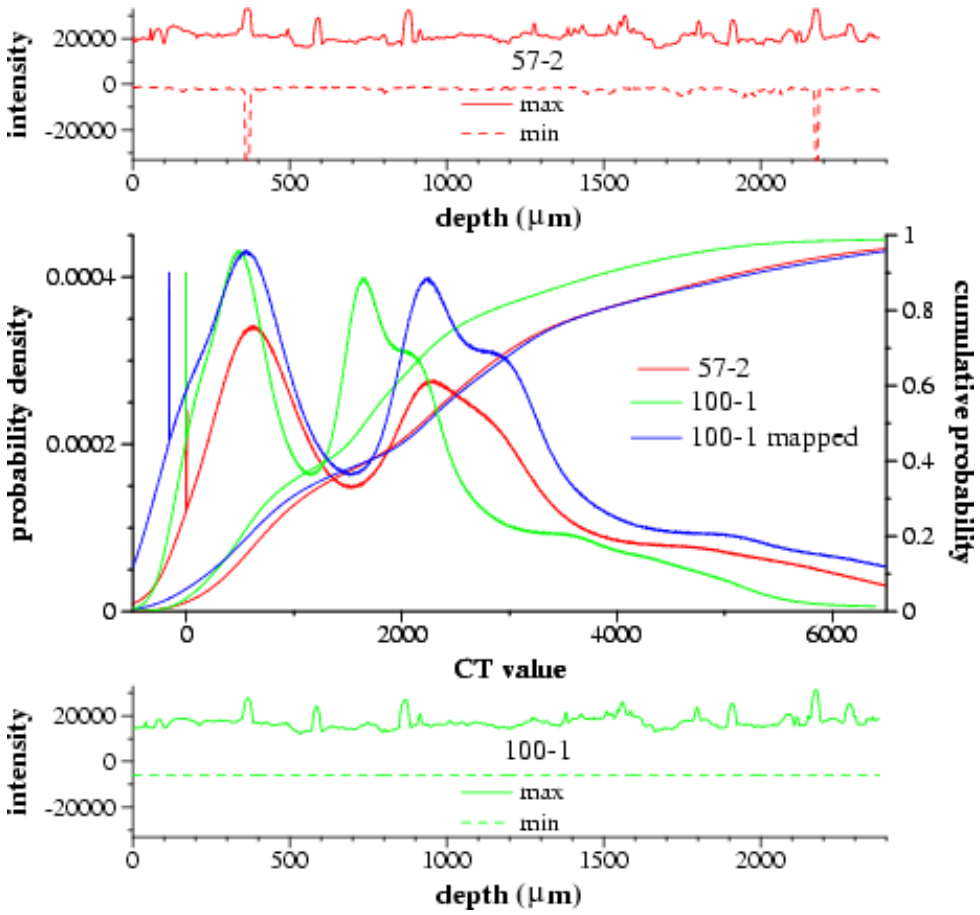

Figure 8: Comparison of CT value histograms for two of the three images analyzed in column section C2. (Top, Bottom plot) CT value ranges for each single slice. (Middle plot) Histogram and cumulative distribution plots for image 57-2 (red trace), 100-1 (green trace) and 100-1 after linear mapping (blue trace).

in the CT value histogram plot) and standard deviation. The change in X-ray energy has the effect to change the mean and deviation parameter in different runs. CT values, E_1, E_2, E_3, corresponding (respectively left to right) to these three extrema were determined from the 57-2 distribution. Corresponding values $E_1^{'}$, $E_2^{'}$, $E_3^{'}$ were determined from the 100-1 distribution. With consistent setting of experimental parameters, the corresponding E, $E^{'}$ values should be identical. (There would be some shift with a change in porosity, but this should be minor.) We assume that the difference in distributions under the 10% shift in X-ray energy used for these two images can be compensated for by a linear map, $E' = m\ E+b$. Three successive pairs of values (E_1, E_2 and $E_1^{'}$, $E_2^{'}$), (E_1, E_3 and $E_1^{'}$, $E_3^{'}$) and (E_2, E_3 and $E_2^{'}$, $E_3^{'}$) were then sampled to determine values for slope, m, and intercept, b, for this linear map. Mean values for the three slopes (and for the three intercepts) determined were used to fit the final linear map $E \rightarrow E^{'}$. Operating on the CT value distribution for 100-1 (green curve) using the linear map, produces the mapped distribution (blue curve). As can be seen, the extrema in the mapped 100-1 distribution and in the 57-2 distribution now line up well. As further test of the quality of the map, the middle figure also plots the cumulative distributions for the CT values. The cumulative distributions for 57-2 and the linearly mapped 100-1 align very well. The linear map was applied to the T_0 and T_1 values used in the segmentation of image 57-2 to select the T_0 and T_1 values used in the segmentation of image 100-1.

For additional evaluation of the experimental image, the range (maximum and minimum values) of CT value in each slice are plotted with respect to depth in the top (for 57-2) and bottom (for 100-1) figures of Fig. 8. No notable systematic trend with depth is seen in these data, indicating stable beam energy over the depth of the sample. There are however two depths ($\sim$365 and $\sim$2180 μm) where abnormally low CT values are encountered in a

section of 4 to 5 contiguous slices. These values are isolated and may be due to temporary pixel faulting in the CCD camera.

Analogous corrective linear maps were used for each region analyzed, correcting the CT value distributions for runs 1 to 4, to match those for run 0.

2.4.2 Image registration

In order to compare the same sections of the column in different runs, it is necessary to assure that the sections are precisely aligned. However, since the column was shipped repeatedly and moved back and forth from PNNL and BNL, this registration could not be accomplished during the imaging, but has to be accomplished by post registration of the images.

In order to avoid possible effects from the region exterior to the column, a fiducial polygon has been imposed on the image to create a region of interest (ROI) within each slice. This ROI defines the region interior to the column that is to be analyzed. In addition to set the same center and radius of the ROI for the same section of the column in the different runs, the individual reconstructed slices had to be rotated about the center of the ROI to align features. We used bilinear interpolation to produce the rotated images.

Two segmented data sets were first roughly aligned vertically using the recorded vertical movement of the column during image taking and rotationally by eye using visibly distinctive grain features. They are then aligned algorithmically by a registration search that minimizes voxel-by-voxel differences amongst all small translational and rotational offsets about the rough alignment position of the two segmented files.

For each slice of section C2, run 3 (114-4), the registration algorithm performed translations through a window of 15 (x-direction) $\times$ 15 (y-direction) $\times$ 11 (z-direction) voxels in size and 7° in rotatonal alignment in the roughly

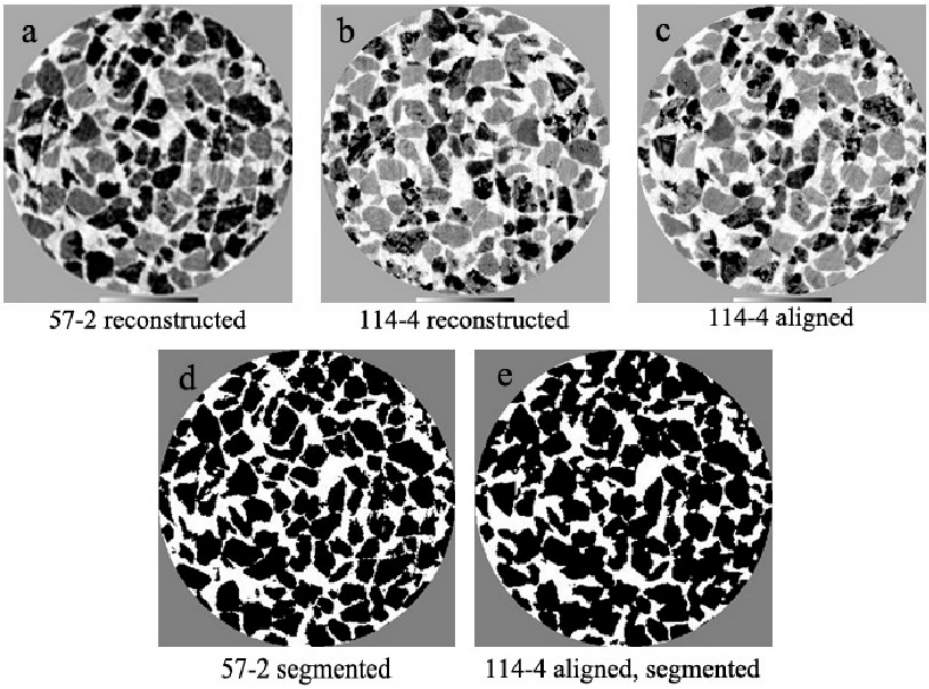

Figure 9: (Top row) Reconstructions of the middle slice of section C2 in run 0(57-2) and run 3(114-4). the slice in run 3 is shown before and after rotational alignment (131° clockwise) with run 0. (Bottom row) The segmented images of the aligned slices.

aligned C2 section of run 0. Note that rotation only occurred around a single axis, the z-axis perpendicular to the plane of the slices. For each translation offset, the voxels whose segmentation matched within the two image ROIs at every rotation angle are counted. The best rotation angle that minimized the difference, as well as the value of the corresponding minimum difference were recorded for each translation. The final registration parameters were determined from the overall minimum difference value.

Fig. 9 compares the reconstructed and segmented image of a single aligned slice midway down section C2 in the images from run 0 and run 3. The image from run3 was translated to align with the same slices from run 0. After the appropriate alignment, the final ROI of the images are defined as the setting of ROIs in both images (translated and rotated).

The careful translational and rotation registration was done, not simply to ensure that the same region is followed through time, but to protect against possible systematic effects in algorithms of the subsequent software analysis. For example, the algorithm [27] that generates the medial axis search path used by the throat finding algorithms has known susceptibilites to angular orientation. For example, the medial axis generated for a digitized cylindrical rod of constant cross section varies somewhat in length depending on the orientation of the rod with respect to the digitization axes. Although all dead end paths, for which (one end of) the digitized rod is an analog, were trimmed from the medial axis before searching for throats, it is possible that there are other direction-dependent systematics in the algorithms used by 3DMA-Rock to analyze the data. Rotating all samples to the same orientation reduces the influence of any such systematics. For the analysis of each section (C1-C4), run 1 through 4, were registered to align with run 0.

2.5 Medial Axis (MA) Extraction and Modification

The medial axis of a digitized object is constructed by eroding an object's voxels layer by layer while preserving its topological and geometric properties. The purpose of finding the medial axis of a three-dimensional object is to obtain a lower dimensional representation that is easier to analyze. 3DMA-Rock implements the Lee-Kashyap-Chu algorithm [27] for the MA extraction in the pore space. The resulting MA set of voxels is formed of digitized curves (paths, links, branches) and digitized versions of vertices (branch clusters, nodes). A modification of this MA set is performed to achieve a 1-1 correspondence of paths and branch clusters with physical channels and pores. This modification includes eliminating dead-end paths (paths that are incident to only one branch cluster) which correspond to dead-end channels and do not contribute to the percolating fluid pathways of the void space ,reducing surface remnant structures and needle-eye paths and merging the branch clusters that lie within the same pore body [32].

The final modified MA set of voxels provides a searchable network for the throat finding algorithm.

2.6 Throat Finding Algorithm

Throats are very important in the research of flow in porous media, since the geometry of throated channels determines the hydraulic conductance and control the flow. Traditional network models represent a channel as an ideally shaped cylinder that connects neighboring pores and has a specific length and cross-sectional area. This method simplifies the 3D space while sacrifices some characteristics from the real geometry.

In our network model, we characterize the pore space as a network of pores and throats with an identified neighbor relationship. A throat, in our definition, is the minimum cross area that connects each pair of neighboring pores along the path channel. As a result of the modifications done in Section 2.5, throat finding occurs along each MA path. Three throat finding algorithms are coded into 3DMA-Rock.

The first is a Dijkstra-based shortest length algorithm [32]. This algorithm keeps dilating each MA path orthogonal to its length, forming a topological cylinder whose surface ultimately contacts solid phase voxels. The first closed loop of solid contact voxels encircling the cylinder is treated as the throat perimeter. The MA path voxel having closest average distance to these perimeter voxels is declared as the throat center. The throat surface is constructed from a triangulation using the perimeter voxels and throat center voxels as vertices. The Dijkstra algorithm is computationally expensive, especially in the porous media sample of high porosity.

This shortcoming of the Dijkstra algorithm inspired the development of the second throat finding algorithm, wedge-based algorithm [55]. It searches roughly formed cross section perimeters (one for each path voxel) and finds the rough cross section area having minimal area. The construction of the approximate perimeters is aided by a precomputation of the local grain boundary (LGB) which determines the set of grain surface voxels that lie closest to any given MA path. For each voxel v on the MA path, a cylindrical coordinate system is constructed based upon the direction tangential to the path at v and a normal direction determined by the LGB voxel closest to v. This cylindrical coordinate system is divided into a finite number of angular wedges, and a perimeter voxel chosen in each wedge using the closest LGB voxel lying within the angular limits determined by the wedge. This set of wedge determined perimeter voxels forms an approximate perimeter which, together with v, can

be triangulated to form a surface. This algorithm is fast; however, it has low success rate in the rock samples with high porosity ($\geq 30\%$), where the throats are relatively wider.

For the media of low porosity ($< 30\%$), it is sufficient to use either of the above two algorithms to obtain a full set of throats. When dealing with a sample of high porosity, such as the Hanford soil sample in this reaction flow experiment (porosity around 30% - 35%), it can be problematic to determine meaningful local minimum along every MA path and the throat finding success rate is usually low. Thus we applied an aggressive throat finding computation as follows:

1) The image volume was first padded by an external grain layer on all sides. The throat finding algorithms usually fail on the MA paths that are cut by the boundary since there is inadequate information to find the correct throats. In the high porosity samples, this problem can have profound effects on pore partition. Missing throats on the boundary truncated channels can produce a huge pore which may extend along all 6 boundaries of the whole image, which contains more than half of the whole pore volume. By introducing the artificial grain boundary on all sides, more boundary throats were detected. As a result, more accurate pore partitioning in finite sized image samples was obtained.

2) The wedge base algorithm was first employed on all the medial axis path due to its speed. This step could find throats on more than half of the MA paths.

3) The Dijkstra search, which is slower, was then used to search for the throats on the medial axis paths where the wedge algorithm failed.

4) Finally, we applied a sub-sectional Dijkstra search [47] to subdivide the

Sample	Porosity(%)	throat detection method	success rate (%)
Run 0	35.26%	wedge	68.7%
		Dijkstra	7.7%
		Subsection	5.08%
		Total	81.51%
Run 3	34.47%	wedge	71.41%
		Dijkstra	7.51%
		Subsection	4.78%
		Total	83.7%
Run 4	31.96%	wedge	80.17%
		Dijkstra	6.26%
		Subsection	3.11%
		Total	89.55%

Table 3: Aggressive throat computation results of X2B Hanford reactive column, C2 section, at run 0, run 3 and run 4. The images of run 3 and run 4 were properly aligned to the image of run 0. The success rate is the rate that throat finding algorithm successfully detects the throat on the MA path.

remaining difficult MA paths and run the Dijkstra search on each segment.

The final set of throat was the union of throats found from step 2)-4).

Table. 3 lists the throat finding success rates of the Hanford soil column samples.

2.7 Pore Throat Network Construction

Network models represent the void space of a rock as a simplified lattice of pores connected by channels. The description of network models have been developed with the technology. Prior to the development of high energy X-ray computed micro-tomography (CMT) in the late 1980's and its rapid improvement in the 1990's, experimental measurement of the distribution of any geometrical measure of pore space in rock was limited either to two dimension thin sections, or to 3D views produced by thin section stacks obtained in the

laboratory through micro-polishing. The X-ray computed tomographic imaging technology now provides a way to produce 3D image sets of rock samples and make it possible to represent the complex geometry and topology of the pore space more accurately.

In our network model, we require that each throat connects (separates) exactly two distinct pore bodies. Thus, for every throat found by the throat finding algorithm, we need to identify the two pore spaces that it separates. However, identification of this pore-throat network is challenging due to the complexity of the geometry when the porosity of the porous media is high. The following problems could occur:

1. throats that intersect two or more MA paths;
2. throats that intersect branch clusters;
3. throats that touch or cross.

These problems can be resulted from throats that are either artifact or physical.

3DMA-Rock has the capacity to remove the problematic throats that are connected to more than 2 pore bodies, the detailed algorithm is described in [47]

The idea of our network construction algorithm is to use the iteration to eliminate all the problematic throats. The rule is to keep as many throats in the network as possible while necessary, abandon the throats that have larger area.

A grass fire algorithm is first used in the pore space to identify individual pores. Throats that separate two distinct pores are retained. Throats that connect to more than two pores are tagged and sorted by the area. Starting from the smallest of this tagged group of throats ,the algorithm checks whether the throat contacts with any other throat that has been retained in the network. If not, it would be untagged and kept in the network. The above

steps of throat selections are repeated on the set of throats that have been kept in the network until all the throats in the network only connect to 2 pore components.

Chapter 3

Effluent Concentration and Micro/Macro-structure Changes Induced by the Reactive Flow

3.1 Effluent Concentrations

Hanford soil contains a number of mineral phases that undergo dissolution in hyperalkaline and saline solutions [51]. Based upon previous experiments [2, 7, 10], our experiment set-up, and analysis of effluent concentrations, we are confident that the dominant reactions occurring in the flow column were dissolution of quartz, producing silicic acids, and precipitation of, predominantly, the sodium aluminosilicates: Linde type A zeolite, nitrate-sodalite, and nitrate-cancrinite. Batch experiments have shown that the endmember, cancrinite, precipitates after 2-10 days [7].

Fig. 10 plots measured concentrations of Al and Si in the solution eluted from the column. The time period on the x-axis has been compressed to show only the elapsed time over the periods (runs 1-4) during which caustic solution flowed through the column. Between runs, the column (and the fluid

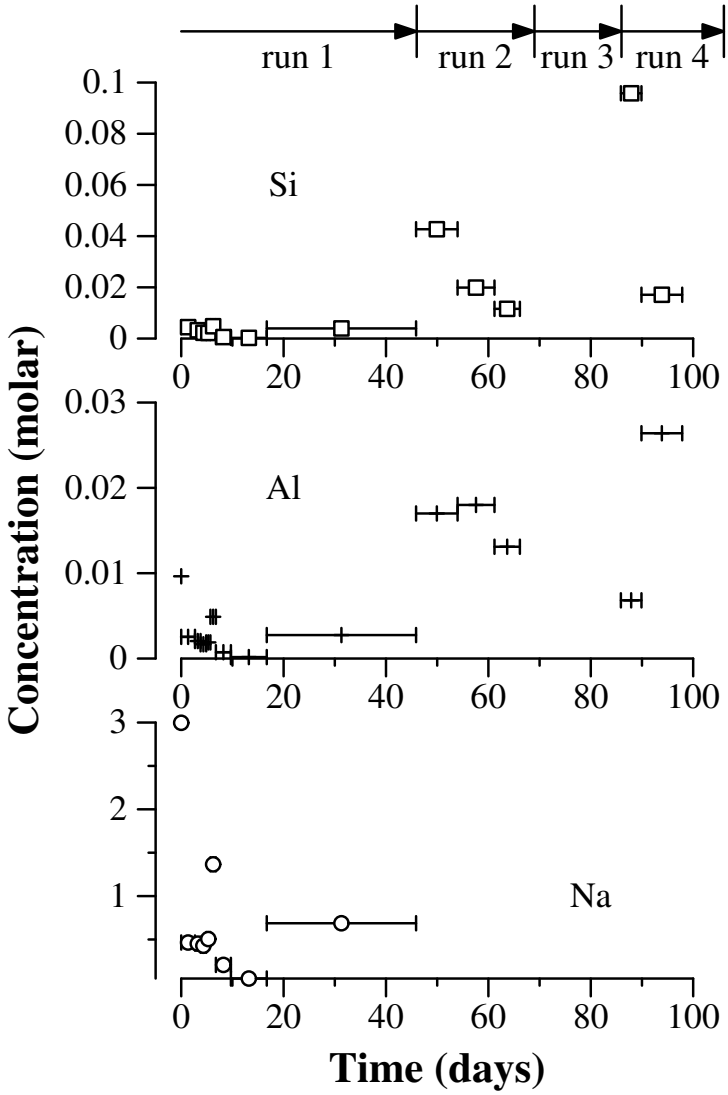

Figure 10: Observed effluent concentrations for Al and Si from the column experiment. Effluent collected over varying periods of time was analyzed; in each case the measured concentration represents averaged accumulation over the time period. The horizontal bar accompanying each measurement indicates the period of time of effluent accumulation contributing to the measurements.

it contained) was sealed (for shipping to BNL for imaging) and reactions within the core continued. Sealed periods varied from 3 to 6.5 months (Table 1).

Si and Al concentration behavior during the first 16 days of run 1 is qualitatively consistent with the flow-column observations of Um and Serne [64]. This behavior indicates an initial period of primary dissolution followed by sodium aluminosilicate precipitation. We note that the last data point in run 1, averaging effluent concentrations over the final 29 days of the run, indicates a "rebound" in which dissolution appears once again to dominate.

During the sealed periods between runs, the column acted like a batch reactor and species depletion should affect the chemistry differently than during the periods of active flow. Batch experiments on Hanford soils [51] indicate that, with input Al concentration of 0.01 M, high Si concentrations (due to precipitation) should be expected at the end of the shut in period. As we cannot take any concentration measurements during the sealed period, such expectation can only be inferred from the initial effluent measurement once the next run has begun. As Al is introduced (at 0.05 M concentration) in the injected solution, Al concentrations during the sealed period are more difficult to infer from initial observations on the subsequent injection period. However, the high Si concentration measurements noted at the beginning of runs 2 and 4 are certainly in agreement with strong dissolution occurring during the sealed periods.

During runs 2 and 4, for which a few concentration measurements are available, Si concentratons decreased over the 20-day run period, consistent with precipitation occurring.

3.2 Porosity Changes

The porosity (number of void space voxels over total number of voxels of the ROI) of the four sections were compared using the segmented images. The bulk porosity changes of these sections are summarized in Fig. 11. We

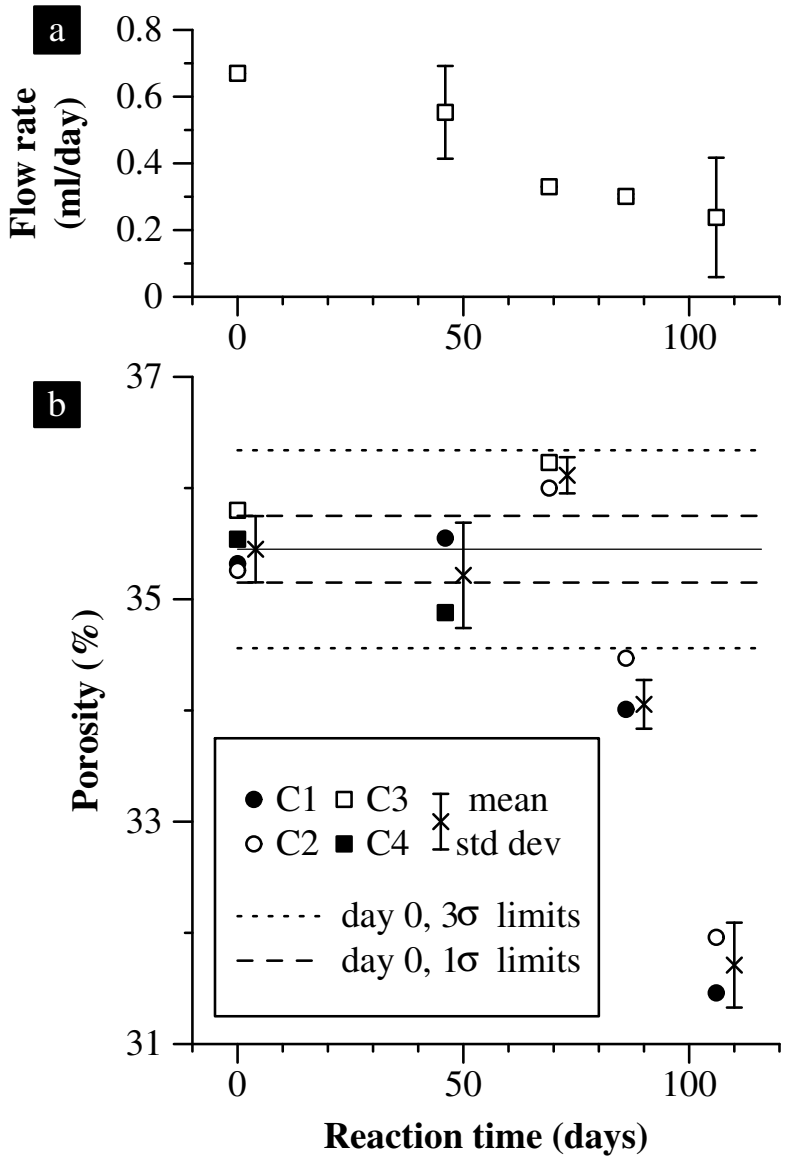

Figure 11: a) Flow rates (mean and one standard deviation) recorded in the column over each run. b) Porosity change measured from the four sectons, C1 → C4, of the column. The horizontal dashed lines indicate 1-standard deviation limits about the average porosity (solid horizontal line) measured for run 0; the horizontal dotted lines indicate 3-standard deviation limits.

use mean and standard deviation values determined from measurements on the four sections at run 0 to determine the significance of any changes at later times. At the level of 1-standard deviation, no net porosity change is evident through 46 days of caustic solution flow; it is possible that dissolution effects temporarily dominated at 69 days. After 86 days, a decrease in porosity (secondary precipitation dominating) is distinctly observed at the 3-standard deviation level. These porosity change results are consistent with the effluent concentration profile trends observed in Fig. 10. Note that, in the caustic fluid environment, precipitated nitrate cancrinite is relatively stable and will not dissolve, thus precipitate accumulates over the lifetime of the observation and reduces the grain surface area that is available for dissolution.

Corroborating evidence for the net dominance of precipitation over dissolution during the time span of the experiment is provided by the changes in flow rate observed in the column with time (Fig. 11(a) and Table 1). With pump settings held constant, the flow rate through the column was observed to fall from an initial rate of 0.67 ml/day ($\sim$2.8 PV/day) to 0.238$\pm$0.179 ml/day ($\sim$1.1 PV/day) after 106 days of caustic waste flow. The rates (average and standard deviation) were based on eluted volume observed for each run. The reduction in flow rate is attributed to precipitate clogging of flow paths, consistent with reduced porosity. Note, there is some discrepancy in the observed porosity and flow rate measured at 69 days.

3.3 Microstructure changes

We quantified the microstructure changes in the pore-scale using the results from our pore-throat network construction.

3.3.1 Pores and throats

Table 4 summarizes the number of pores and throats found in C1 and C2 sections at 0, 86, and 106 days. The data show decreases in the number of pores and throats, by 25% and 38% respectively, after 106 days. This decrease is accompanied by significant shifts in the distribution of pore and throat sizes. Fig. 12(b) displays the measured distributions for pore volume and throat area (data aggregated for the two sections). By 106 days, there was a clear loss of small volume ($< 10^{-4}$ mm^3) pores, and small-area ($< 10^4 \mu$m^2) throats. Table 4 quantifies these changes. After 106 days exposure to flowing caustic fluid, there was a 64% decrease in the number of pores with size less than 1.26×10^{-4} mm^3 and a 42% decrease in the number of throats with size less than 1.19×10^4 μm^2. While the number of large ($>1.19\times10^4$ μm^2) throats remained little changed (Fig. 12, Table 4), there was a 34% increase in the number of large ($>1.26\times10^4$ mm^3) pores (although the overall porosity decreases). We note that in the pore and throat data presented in Table 4 and Fig. 12(a)(b), we include only pores and throats lying completely inside the imaged region of the column. This allows us to base our extracted information on completely resolved pores and throats, and not on bodies truncated artificially by the boundary of the image region or the edge of the column.

3.3.2 Coordination number

The coordination number of a pore is defined as the number of other pores to which it directly connects. In our pore-throat network description, this is equivalent to the number of throats through which a pore connects to others. The coordination number is one of the essential descriptive parameters of the pore space which controls the flow properties of the porous medium. Fig. 12(c) shows how the average coordination number of a pore changed with time as a function of pore size. In this plot, pore size is expressed as an effective radius,

Day	Pores	Pores with volume	
		$< 1.26 \times 10^{-4}$ mm^3	$> 1.26 \times 10^{-4}$ mm^3
0	14668	8801	5867
86	14648	7763	6885
106	11047	3204	7843

Day	Throats	Throats with area	
		$< 1.19 \times 10^4 \mu$ m^2	$> 1.19 \times 10^4 \mu$ m^2
0	35755	32180	3575
86	32524	28621	3903
106	22052	18524	3528

Day	C1		C2	
	Shortest paths	Average tortuosity	Shortest paths	Average tortuosity
0	701190	1.685	627244	1.672
86	540912	1.685	575059	1.680
106	211404	1.701	310240	1.690

Table 4: Characterizations of changes in numbers of pores, throats and paths, as well as path tortuosity, in the analyzed sections C1 and C2. For pores and throats, the statistics from sections C1 and C2 are aggregated.

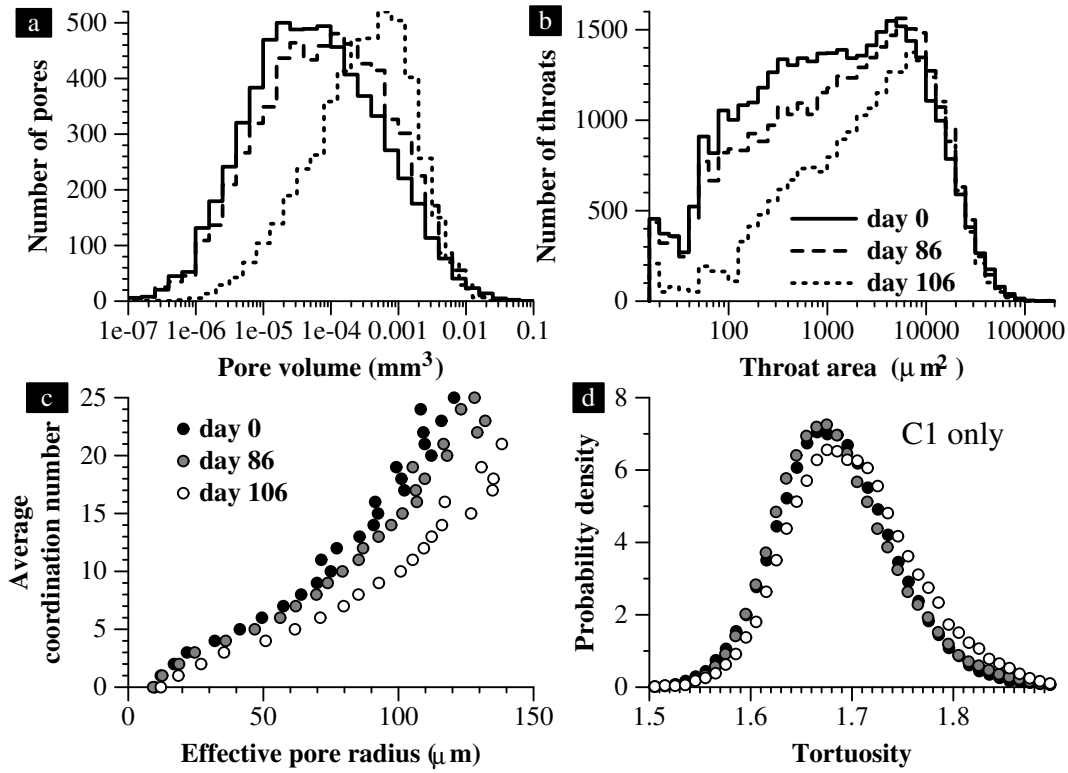

Figure 12: Distributions of (a) pore volume and (b) throat area as well as (c) average pore coordination number vs. effective pore radius determined from sections C1 and C2 after 0, 86 and 106 days of exposure to simulated caustic waste flow. (d) Distribution of pathway tortuosities (section C1 only)

$r_{eff} = (3V/4\pi)^{1/3}$, where V is the measured pore volume. Except for the smallest pores, there was a decrease in the average coordination number for pores of any given size, as small throats closed off due to secondary precipitation. For the large pores (> 90 μm radius), this decrease was largest - on average about 5 throats.

3.3.3 Connectivity and tortuosity

Reactive flow induced changes in porosity may affect the overall connectivity of the pore network. We quantified this effect by considering the medial axis of the pore network [27, 33, 35]. We intersected the medial axis with two parallel planes separated by a distance h (see Fig. 13 for illustration). To avoid looping behavior, we examined the set of shortest paths through the medial axis that connect each medial axis point on one plane with each medal axis point on the other plane. If there are N medial axis points on one plane, and M on the other, there will be at most NM shortest paths through the medial axis connecting such point pairs. The two planes were established at each end of sections C1 and C2 along the column length ($h = 580$ voxels). Table 4 gives the number of shortest paths between the two ends of each section as a function of time. There were 70% (C1) and 50% (C2) decreases in the number of such shortest path connections after 106 days.

We define the geometric tortuosity of a path in the usual manner. Fig. 12(d) displays the distribution of tortuosities measured for these spanning paths; Table 4 presents the average tortuosity values. In spite of the significant decrease in the number of pathways connecting the planes, there was only a slight shift to higher path tortuosities, specifically average tortuosity increased by only 2.3% (C1) and 2.7% (C2). Since tortuosity, τ, must be unity or larger, this percent increase was computed as $(\tau_{106} - \tau_0)/(\tau_0 - 1)$.

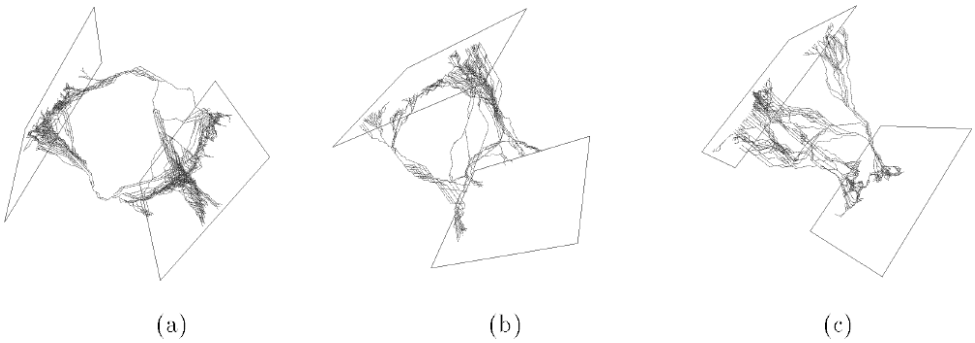

Figure 13: The shortest paths on the medial axis connecting two opposite faces ((a) x-, (b) y-, (c) z-direction) of a 56^3 voxel cubic subregion in a Berea sample. For viewing clarity, each figure has been rotated. Figures at courtesy of [35]

3.4 Discussion

The image analysis results suggest that, for dissolution processes accompanied by secondary precipitation, the dissolution processes dominate in the larger pores while precipitation fills in small pores and clogs small throats. This finding is not qualitatively unexpected. (In fact, this qualitative agreement lends further support for the results.) Certainly precipitation processes need quiescent conditions for nucleation. Such conditions are expected to occur in regions of slow fluid flow associated with (i) angular corners in pores at multi-grain junctions, (ii) small pores and (iii) throats.

The significance of our work is the demonstration of the ability to quantify such changes over a microscale pore-network volume in a non-destructive manner, allowing for repeated measurements over repeated flow conditions and providing basic concepts for predicting contaminant transport in a larger scale. The specific quantitative findings presented in Sections 3.2-3.3 are, of course, based upon a small volume from a single column. Careful experiments under controlled conditions with a larger number of samples are clearly required to extract significant quantitative results for specific reaction processes. This

caution notwithstanding, our results do provide some tantalizing insights. In addition to the expected loss of pore-to-pore connectivity accompanying presumable throat clogging, we recorded a significant decrease in the number of network pathways. In spite of this decrease, there was not a significant increase, on average, in the tortuosity of the remaining pathways. While there was an increase in the number of large pores due to dissolution processes, there was not a corresponding increase in the number of large throats, suggesting that all throating areas are dominated by precipitation processes.

There are specific issues that still need to be addressed regarding the use of CMT imaging on flow-column experiments.

The first is the question of the size of the volume to be examined in order to produce representative results. In earlier work [34], we have demonstated that microgeometrical measurements based on CMT images of 14.8 mm^3 volume are locally representative (produce statistically reproducible results in a core sample) in Fontainebleau sandstones ranging from 7.5% to 22% porosity. While the 17.9 mm^3 images examined here are comparable in size, the REV (Representative Element Volume) requirements to capture the effects of reactive flow remain to be addressed.

The region of the flow-column imaged was close to the mid-length of the column. It would be interesting to compare images taken from the inlet and outlet ends of the column to see if reactive changes are different.

Sealing the column for extensive time periods between runs while waiting for imaging time certainly complicates reaction interpretation. Clearly tight management between the flow-column runs and availability of bean time is required. Experimentally it would be attractive to have the flow column experiment run in a beam line hutch, allowing for the possibility to swing the column into the beam periodically for imaging, without having to halt the flow for any significant amount of time.

Chapter 4

Reactive Network Flow Model

4.1 Reactive Network Flow Model Setup

The XCMT image analysis revealed micro-structure changes induced by the reactive flow in the Hanford flow column experiment consistent with the experiment measured effluent changes and chemical species concentration evolution. This motivated the development of a single phase reactive flow model based on the imaged pore-throat network. The goals of our model are to 1) simulate the transport of chemical species in the flow-column experiment; 2) see to what extent the experiment observation of the effluent chemical species concentration changes can be duplicated.

For each pore in our pore-throat network, we consider the aqueous chemical species evolution as a result of the reactive flow advection via throat channels, aqueous species diffusion to neighboring pores, and surface reaction kinetics. The concentration change rate of chemical species in pore i can be modeled by changes caused by

1. advection

$$V_i \frac{d[\cdot]}{dt}\Big|_{A,i} = \sum_j (-Q_{ij}[\cdot]_i); \tag{1}$$

2. diffusion

$$V_i \frac{d[\cdot]}{dt}\Big|_{D,i} = \sum_j D_{[\cdot]} A_{ij} \frac{[\cdot]_j - [\cdot]_i}{l_i j}; \tag{2}$$

3. kinetic reactions

$$V_i \frac{d[\cdot]}{dt}\Big|_{R,i} = S_p([\cdot]) + S_d([\cdot]). \tag{3}$$

In equation (1)-(3), $[\cdot]$ denotes concentration of a n aqueous species; j is the indexes of pores that neighbor pore i; S_p is the source term for precipitation reactions; S_d is the source term for dissolution reactions; $D_{[\cdot]}$ is the diffusion coefficient of the aqueous species; V_i is the volume of pore i, A_{ij} is the area of the throat that connects pore i to j, and Q_{ij} is the volumetric flow from pore i to j.

Summing equation (1)-(3) establishes an ordinary differential equation for the concentration change rate of each chemical species.

$$V_i \frac{d[\cdot]_i}{dt} + \sum_{Q_{ij}>0} Q_{ij}[\cdot]_j + \sum_{Q_{ij}<0} Q_{ij}[\cdot]_j = S_i[\cdot] + \sum_j D_{[\cdot]} A_{ij} \frac{[\cdot]_j - [\cdot]_i}{l_{ij}}. \tag{4}$$

The coupled pore system (4) numerically by the Euler method to take advantage of its speed.

4.1.1 Single phase network flow model

The reactive flow in the column is pressure driven single phase flow that transports the aqueous species in the pore-throat network

The flow rate Q_{ij} [L^3/T] from pore i to j can be numerically calculated by Darcy's law,

$$Q_{ij} = \frac{g_{ij}}{l_{ij}}(p_i - p_j) \tag{5}$$

where g_{ij} $[L^5T/M]$ is the effective fluid conductance, l_{ij} is the distance between the pore centers, and p_i is the pressure in pore i.

g_{ij} can be equivalently represented as $g_{ij} = k_{ij}A_{ij}/\mu$, where k_{ij} is the channel permeability in Darcy unit, A_{ij} is the cross-section area of the throat channel, and μ is the viscosity of the fluid.

Once throat conductances are computed (details described in Section 4.3), conservation of flow volume determines a system of linear equations for the unknown interior pore pressures. For each pore K, connected to interior pore A,

$$\sum Q_{AK} = \sum \frac{g_{AK}}{l_{AK}}(P_A - P_K) = 0. \tag{6}$$

Regrouping the RHS of (6), and considering the pressure on the inlet and outlet boundaries, (6) can be written as

$$P_A \sum \frac{g_{AK}}{l_{AK}} - \sum_{K_{int}} \frac{g_{AK_{int}}}{l_{AK_{int}}} P_{Kint} = \sum_{K_{in}} \frac{g_{AK_{in}}}{l_{AK_{in}}} P_{K_{in}} + \sum_{K_{out}} \frac{g_{AK_{out}}}{l_{AK_{out}}} P_{K_{out}}, \tag{7}$$

where the subscripts *int*, *in*, *out* stand for interior, inlet and outlet pores respectively. The number of unknowns in the system (7) is equal to the number of interior pores.

System (7), which is sparse and symmetric, was solved by the preconditioned conjugate gradient iteration method. Total in-flow Q and individual flow rates Q_{ij} from pore i to pore j were calculated from the interior pore pressures gradient. The pressure gradient across the system $(p_{in} - p_{out})$ was adjusted to provide the flow rate set by the column experiments.

4.1.2 Diffusion

The diffusion of each aqueous chemical species is described by Fick's Law,

$$J = -D\frac{\partial C}{\partial x}. \tag{8}$$

Here J is the diffusion flux ($\mathrm{L}^{-2}\mathrm{T}^{-1}$), D is the diffusion coefficient ($\mathrm{L}^{2}\mathrm{T}^{-1}$). C is the molar concentration (L^{-3}). The diffusion coefficient is species dependent. It also changes with temperature and pressure. Given the diffusion coefficient D_{T_1} of a species at temperature T_1, the corresponding D_{T_2} at temperature T_2 can be approximated by the Stokes-Einstein equation,

$$\frac{D_{T_1}}{D_{T_2}} = \frac{T_1}{T_2}\frac{\mu_{T_2}}{\mu_{T_1}}, \tag{9}$$

where, μ_{T_1} and μ_{T_2} are the dynamic viscosities of water at temperatures T_1 and T_2.

The diffusion coefficients at $25°C$, and 101.3 kPa for the species involved in our model are listed in Table 7.

4.1.3 Surface (kinetic) reactions

The two surface reactions involved in this simulation are the dissolution of the quartz surface with release of the silicic acid into the fluid, and consumption of the aluminum ions to form the solid cancrinite precipitates. Both processes were modeled kinetically.

1. Dissolution of quartz (silica, SiO_2)

The dissolution of of quartz,

$$SiO_2\ (\text{solid}) + 2H_2O \rightarrow Si(OH)_4\ (\text{aq}), \tag{10}$$

has been studied widely. The reaction rate constant $k_+[\text{mol m}^{-2}\ \text{s}^{-1}]$ at $25°C$

has been measured [69] as dependent on pH value,

$$\log_{10} k_+ = -14.547 \pm 0.162 + (0.361 \pm 0.02)\text{pH}. \tag{11}$$

The pH value for the solution in each pore was updated at each simulation time step in order to updated the local dissolution rate constant. The dissolution rate for each pore was then computed by k_+A, where A is the computed pore surface area, which was corrected by multiplying a coefficient to agree with the BET measured specific area (5.11 m^2/g) of the Hanford soil sample. We assumed that the whole pore surface was available for reaction.

2. Precipitation of Nitrate-Cancrinite ($Na_8Si_6Al_6O_{24}(NO_3)_2{\cdot}4H_2O$)

Batch experiments [7] with simulated reactive solution have been performed to measure the kinetics of precipitation and the conditions under which secondary aluminosilicates might precipitate. Cancrinite, a zeolite-like mineral has been reported to precipitate after reacting with Hanford sediments for 11.7 weeks at 60°C and at 90°C in a complex tank simulate. The kinetics of cancrinite precipitation is described as

$$\begin{aligned} 8\text{Na}^+ + 6\text{Al(OH)}_4^- + 6\text{H}_2\text{SiO}_4^{2-} + 4\text{NO}_3^- \leftrightarrow \\ \text{Na}_8\text{Si}_6\text{Al}_6\text{O}_{24}(\text{NO}_3)_2 \cdot \ 4(\text{H}_2\text{O})(\text{s}) + 12\text{OH}^- + 8\text{H}_2\text{O}, \end{aligned} \tag{12}$$

for which a measured precipitation rate, normalized to 1 kg H_2O solution, is

$$1.03 \pm 0.05 \times 10^{-6}[\text{Al}]^{1.22}[\text{Si}]^{0.23} \text{ mol cancrinite } \text{s}^{-1}. \tag{13}$$

This secondary precipitation won't occur until the dissolved silica concentration increases and the solution becomes supersaturated with respect to an aluminosilicate phase. Supersaturation status is measured relative to the equilibrium constant, K_{eq},

$$K_{eq} = \frac{\{OH^-\}^{12}}{\{Na^+\}^8\{Al(OH)_4^-\}^6\{H_2SiO_4^{2-}\}^6\{NO_3^-\}^2}, \tag{14}$$

where $\{\cdot\}$ indicates activities at equilibrium conditions. We used the experiment measured value $\log_{10}K_{eq} = 36.2$ from [7]

At each simulation time step, we calculated the saturation index Ω for each pore.

$$\Omega = \frac{K_{eq}\{Na^+\}^8\{Al(OH)_4^-\}^6\{H_2SiO_4^{2-}\}^6\{NO_3^-\}^2}{\{OH^{-12}\}}. \tag{15}$$

If and only if $\Omega > 1$ ($\log_{10}\Omega > 0$) in a pore, the solution is locally supersaturated and precipitation occurs.

The concentration change of each species involved in the dissolution/precipitation was computed in each pore using the local reaction rate and updated at each simulation time step.

4.1.4 Instantaneous reactions of the aqueous species

The (time varying)solution of (18) doesn't guarantee equilibrium of chemical species. After each time step, we need to incorporate an instantaneous equilibrium computation for all species.

We model 7 instantaneous aqueous reactions and 11 aqueous species. Table 5 lists the equations for these reactions and corresponding reaction constants. Both Na^+ and NO_3^- are not considered here, since they are not involved in these instantaneous reactions. The equilibrium computation of the species concentrations was computed following the kinetic reaction computation during each simulation time step.

By applying the logarithm, the activity equilibrium equations can be transformed to linear equations. Therefore, we establish a system of linear equations, with 11 unknown $\log_{10}\{\text{species}\}$. The first step is to find the smallest set

	Derived reactions	$\log K_{eq}$	Activity equilibrium equations
1.	$H_2O\text{-}OH^-=H^+$	-13.2	$\{H^+\}=K_1\{H_2O\}\{OH^-\}^{-1}$
2.	$Al(OH)_4^-\text{-}OH^-= Al(OH)_3$	-7.6	$\{Al(OH)_3\}=K_2\{Al(OH)_4^-\}\{OH^-\}^{-1}$
3.	$Al(OH)_4^-\text{-}2OH^- = Al(OH)_2^+$	-13.8	$\{Al(OH)_2^+\}=K_3\{Al(OH)_4^-\}\{OH^-\}^{-2}$
4.	$Al(OH)_4^-\text{-}3OH^-=Al(OH)^{2+}$	-21.85	$\{Al(OH)^{2+}\}=K_4\{Al(OH)_4^-\}\{OH^-\}^{-3}$
5.	$Al(OH)_4^-\text{-}4OH^-=Al^{3+}$	-30.1	$\{Al^{3+}\}=K_5\{Al(OH)_4^-\}\{OH^-\}^{-4}$
6.	$H_2SiO_4^{2-}+H_2O\text{-}OH^- = H_3SiO_4^-$	0.03	$\{H_3SiO_4^-\}=K_6\{H_2SiO_4^{2-}\}\{OH^-\}^{-1}$
7.	$H_2SiO_4^{2-}+2H_2O\text{-}2OH^-=H_4SiO_4$	-3.4	$\{H_4SiO_4\}=K_7\{H_2SiO_4^{2-}\}\{OH^-\}^{-2}$

Table 5: Instantaneous reactions and equilibrium constants at $25°C$ and 1 atm. The reaction equations are written for all the secondary species as a function of the components. Notice that the item of $\{H_2O\}$ is omitted in the activity equilibrium equations, since its activity is always equal to 1 in the computation.

of independent species characterizing the chemical system, which is defined as components [4]. The number of species in this set should equal to the rank of the coefficient matrix of this system. Then the $\log_{10}$ activity of all remaining (secondary) species can be represented as the linear combination of the $\log_{10}$ activity of these components.

The choice of components is not unique. Here, we chose H_2O, OH^-, $Al(OH)_4^-$, and $H_2SiO_4^{2-}$ as the components. This choice of set of components are for the sake of equilibrium computation convenience, which we will discuss later in this section.

From [4], we know that at any time during the equilibrium reactions, masses of each species are not conserved. Instead, the equilibrium state governs the mass balance of the species. This mass balance of the species guarantees that the mass of any element can not be changed by the aqueous reactions. For example, whenever one mole of Al^{3+} is produced, 1 mole of $Al(OH)_4^-$ is consumed. Thus, the total mass of Al element keeps unchanged. The mass balance in our system can be described by the conservation of the total concentration of the 4 components during the aqueous reactions. Table 6 lists the total concentrations of all components.

Components	Total concentration
H_2O	$[H_2O]+[H^+]+[H_3SiO_4^-]+2[H_4SiO_4]$
OH^-	$[OH^-]$-$[H^+]$-$[Al(OH)_3]$-$2[Al(OH)_2^+]$-$3[Al(OH)^{2+}]$-$4[Al^{3+}]$-$[H_3SiO_4^-]$-$2[H_4SiO_4]$
$Al(OH)_4^-$	$[Al(OH)_4^-]+[Al(OH)_3]+[Al(OH)_2^+]+[Al(OH)^{2+}]+[Al^{3+}]$
$H_2SiO_4^{2-}$	$[H_2SiO_4^{2-}]+[H_3SiO_4^-]+[H_4SiO_4]$

Table 6: Total concentration expressions of all four components

We explain how the total concentration is found using the example of component H_2O. The equilibrium reactions involving H_2O are reactions 1, 6, and 7 in Table 5. When one mole of H^+ is produced, 1 mole of H_2O is consumed (reaction 1). Likewise, when 1 mole $H_3SiO_4^-$ is produced, 1 mole H_2O is consumed (reaction 6); when 1 mol H_4SiO_4 is produced, 2 moles of H_2O are consumed (reaction 7). Thus at any time during the equilibrium reactions, the total moles of the species H_2O + H^+ + H_3SiO_4 + 2 H_4SiO_4 remains constant. The sum of the concentrations of these species is then the total concentration of component H_2O.

Table 7 lists the complete information for the equilibrium computation of the 7 instantaneous reactions. The information of the components are listed in the first four rows; the remaining rows are for 7 secondary species, which contain the exponents and equilibrium contans of the derived equilibrium equations in Table 5. The columns of components in Table 7 provide the species and coefficients for the total concentrations of components.

The total concentration of the components can be computed using Table 5, given the concentration of each species. It's critical to find the concentration of each species that satisfies both mass balance and activity equilibrium. We know that concentration of one species is related to its activities by an activity coefficient γ, $[\cdot] = \{\cdot\}/\gamma$. Thus we can rewrite the expression of total concentration by activities of the species. For example, $TOT[H_2O] = \{H_2O\}/\gamma_{H_2O}+\{H^+\}/\gamma_{H^+}+\{H_3SiO_4^-\}/\gamma_{H_3SiO_4^-}+\{H_4SiO_4\}/\gamma_{H_4SiO_4}$. (Note that

activity coefficients are solution dependent. In this work, activity coefficient is computed by Davis' equation [4] (see Section 4.4.3 for details).)

Therefore, the problem of equilibrium reaction computation is reduced to finding the activity of all the species satisfying the linear system,

$$\begin{cases} \mathrm{TOT}[\mathrm{H_2O}](t) &= \mathrm{TOT}(\mathrm{H_2O})(t_0) \\ \mathrm{TOT}[\mathrm{OH^-}](t) &= \mathrm{TOT}(\mathrm{OH^-})(t_0) \\ \mathrm{TOT}[\mathrm{Al(OH)_4^-}](t) &= \mathrm{TOT}(\mathrm{Al(OH)_4^-})(t_0) \\ \mathrm{TOT}[\mathrm{H_2SiO_4^{2-}}](t) &= \mathrm{TOT}(\mathrm{H_2SiO_4^{2-}})(t_0) \\ \log_{10}\{\mathrm{H^+}\} &= \log_{10}K_1 + \log_{10}\{\mathrm{H_2O}\} - \log_{10}\{\mathrm{OH^-}\} \\ \log_{10}\{\mathrm{Al(OH)_3}\} &= \log_{10}K_2 + \log_{10}\{\mathrm{Al(OH)_4^-}\} - \log_{10}\{\mathrm{OH^-}\} \\ \log_{10}\{\mathrm{Al(OH)_2^+}\} &= \log_{10}K_3 + \log_{10}\{\mathrm{Al(OH)_4^-}\} - 2\log_{10}\{\mathrm{OH^-}\} \\ \log_{10}\{\mathrm{Al(OH)^{2+}}\} &= \log_{10}K_4 + \log_{10}\{\mathrm{Al(OH)_4^-}\} - 3\log_{10}\{\mathrm{OH^-}\} \\ \log_{10}\{\mathrm{Al(OH)_2^+}\} &= \log_{10}K_5 + \log_{10}\{\mathrm{Al^{3+}}\} - 4\log_{10}\{\mathrm{OH^-}\} \\ \log_{10}\{\mathrm{H_3SiO_4^-}\} &= \log_{10}K_6 + \log_{10}\{\mathrm{H_2SiO_4^{2-}}\} + \log_{10}\{\mathrm{OH^-}\} \\ \log_{10}\{\mathrm{H_4SiO_4}\} &= \log_{10}K_7 + \log_{10}\{\mathrm{H_2SiO_4^{2-}}\} - 2\log_{10}\{\mathrm{OH^-}\} \end{cases}, \tag{16}$$

The equilibrium coefficients K_1 to K_7 are given in Tables 5 and 7.

This 11×11 equation system, (16), could be numerically solved by e.g. Newton Raphson method. However, in this work, our choice of components enabled us to lower the dimension of the problem to a single variable linear equation, which improved the stability of the system and was faster and simpler in computation.

As noted in the activity equilibrium equations, $\mathrm{OH^-}$ is the only component that is related to the activity of all the secondary species while the other three components are not directly coupled with each other. We can the following substitution for the total concentration expressions.

$$
\begin{aligned}
\mathrm{TOT}[\mathrm{H_2SiO_4^{-2}}] &= \mathrm{TOT}[\mathrm{H_2SiO_4^{-2}}]_0 \\
&= [\mathrm{H_2SiO_4^{-2}}] + [\mathrm{H_3SiO_4^{-}}] + [\mathrm{H_4SiO_4}] \\
&= \frac{\{\mathrm{H_2SiO_4^{-2}}\}}{\gamma_{\mathrm{H_2SiO_4^{-2}}}} + \frac{\{\mathrm{H_3SiO_4^{-}}\}}{\gamma_{\mathrm{H_3SiO_4^{-}}}} + \frac{\{\mathrm{H_4SiO_4}\}}{\gamma_{\mathrm{H_4SiO_4}}} \\
&= \frac{\{\mathrm{H_2SiO_4^{-2}}\}}{\gamma_{\mathrm{H_2SiO_4^{-2}}}} + \frac{K_6\{\mathrm{H_2SiO_4^{2-}}\}}{\gamma_{\mathrm{H_3SiO_4^{-}}}\{\mathrm{OH^-}\}} + \frac{K_7\{\mathrm{H_2SiO_4^{2-}}\}}{\gamma_{\mathrm{H_4SiO_4}}\{\mathrm{OH^-}\}^2} \\
&= \{\mathrm{H_2SiO_4^{-2}}\}\left(\frac{1}{\gamma_{\mathrm{H_2SiO_4^{-2}}}} + \frac{K_6\{\mathrm{OH^-}\}^{-1}}{\gamma_{\mathrm{H_3SiO_4^{-}}}} + \frac{K_7\{\mathrm{OH^-}\}^{-2}}{\gamma_{\mathrm{H_4SiO_4}}}\right).
\end{aligned} \tag{17}
$$

Thus,

$$
\begin{aligned}
\{\mathrm{H_2SiO_4^{2-}}\} =& \mathrm{TOT}[\mathrm{H_2SiO_4^{-2}}]_0 \\
&\cdot \left(\frac{1}{\gamma_{\mathrm{H_2SiO_4^{-2}}}} + \frac{K_6\{\mathrm{OH^-}\}^{-1}}{\gamma_{\mathrm{H_3SiO_4^{-}}}} + \frac{K_7\{\mathrm{OH^-}\}^{-2}}{\gamma_{\mathrm{H_4SiO_4}}}\right)^{-1}.
\end{aligned} \tag{18}
$$

.

Similarly, we can get

$$
\begin{aligned}
\{\mathrm{Al(OH)_4^{-}}\} =& \mathrm{TOT}[\mathrm{Al(OH)_4^{-}}]_0\left(\frac{1}{\gamma_{\mathrm{H_2SiO_4^{-2}}}} + \frac{K_2\{\mathrm{OH^-}\}^{-1}}{\gamma_{\mathrm{Al(OH)_3}}}\right. \\
&\left. + \frac{K_3\{\mathrm{OH^-}\}^{-2}}{\gamma_{\mathrm{Al(OH)_2^{+}}}} + \frac{K_4\{\mathrm{OH^-}\}^{-3}}{\gamma_{\mathrm{Al(OH)^{2+}}}} + \frac{K_5\{\mathrm{OH^-}\}^{-4}}{\gamma_{\mathrm{Al^{3+}}}}\right)^{-1}.
\end{aligned} \tag{19}
$$

From equations (18) and (19), we were able to compute the activity of all the components from $\mathrm{TOT}[\mathrm{Al(OH)_4^{-}}]_0$ and $\mathrm{TOT}[\mathrm{H_2SiO_4^{2-}}]_0$, given $\{\mathrm{OH^-}\}$. Therefore we converted the problem into finding the value of $\{\mathrm{OH^-}\}$ which satisfies the conservation of $\mathrm{TOT}[\mathrm{OH^-}]$, namely $\mathrm{TOT}[\mathrm{OH^-}] = \mathrm{TOT}[\mathrm{OH^-}]_0$.

Define $f(\{\mathrm{OH^-}\}) \equiv \mathrm{TOT}[\mathrm{OH^-}](t) - \mathrm{TOT}[\mathrm{OH^-}]_0$, the root of the equation $f(\{\cdot\})$ is exactly the activity that satisfies the conservation condition. The secant method was applied for finding the numerical solution to $f(\{OH^-\})$.

	H_2O	OH^-	$Al(OH)_4^-$	$H_2SiO_4^{2-}$	$\log K_{eq}$	z	D	M
1.H_2O	1	0	0	0	0.0	0	0.0e0	18.02
2.OH^-	0	1	0	0	0.0	-1	5.3e-9	17.01
3.$Al(OH)_4{}^-$	0	0	1	0	0.0	-1	1.0e-9	95.01
4.$H_2SiO_4^{2-}$	0	0	0	1	0.0	-2	8.0e-10	94.10
5.H^+	1	-1	0	0	-13.2	1	9.31e-9	1.01
6.$Al(OH)_3$	0	-1	1	0	-7.6	0	1.5e-9	78.00
7.$Al(OH)_2^+$	0	-2	1	0	-13.8	1	1.2e-9	61.00
8.$Al(OH)^{2+}$	0	-3	1	0	-21.85	2	8.0e-10	43.99
9.Al^{3+}	0	-4	1	0	-30.1	3	5.6e-10	26.98
10.$H_3SiO_4^-$	1	-1	0	1	0.03	-1	1.2e-9	95.11
11.H_4SiO_4	2	-2	0	1	-3.4	0	1.7e-9	96.12

Table 7: Parameters used in the equilibrium computation

4.2 Initial and Boundary Conditions

The simulation domain is defined by the ROI imposed on each image section analyzed. The domain is thus a vertical cylinder with side boundaries defined by the ROI. Initially, the pore space was filled by ground water of pH 6.6. The reactive fluid was injected from the top at a constant rate.

We used the same parameters as the experiment for the inflow solution. The concentration of the reactive fluid was, $[Na^+]$ = 2.2M, $[Al^{3+}]$ = 0.05M, $[OH^-]$ 1.2M, NO_3= 1.15M. The total volumetric flow rate was set as 2.560810^{-12} m^3/s based on the cross section area of the domain. The top and bottom pressure difference was computed to ensure the total flow rate.

In the simulation, we assumed that geometry changes were not significant and would not affect the permeability of the domain and hydraulic conductance of each throat channel. Given the constant total flow rate from the inlet, the flow rate for each pore was therefore unchanged throughout the time. This assumption, however was not consistent with our XCMT image analysis results. It is our ultimately goal to incorporate these geometric changes in the reactive model. Yet, this part is beyond the scope of discussion in this thesis

work.

4.3 Channel Conductances Computation

Throat channel conductances computation is important in simulating flow advection. We discuss two different models here, the traditional shape factor model, and a LB computation based power-law model. Here, we discuss andcompare the channel conductances computation results from both model.

4.3.1 Shape factor model

A standard computation for the effective conductance, g_{ij}, is as the harmonic mean of the conductances of the connecting throat (channel) and the two pore bodies,

$$\frac{l_{ij}}{g_{ij}} = \frac{l_t}{g_t} + \frac{1}{2}[\frac{l_i}{g_i} + \frac{l_j}{g_j}], \tag{20}$$

where the subscript t stands for throat. The lengths l_α, $\alpha = i, j, t$, associated with pore bodies i and j and the connecting throat t, satisfy

$$l_{ij} = l_t + \frac{1}{2}(l_i + l_j). \tag{21}$$

The length l_α and the corresponding conductances g_α must be modeled. A typical way to model these conductances is to use geometric simplifications of the cross sectional shape of pore bodies and throats as one of three categories, triangle, regular polygon and ellipse. For these shapes, the dimensionless conductance $\tilde{g} \equiv g\mu/A^2$ is monotonically related [45] to the dimensionless shape factor [37] $G \equiv A/P^2$. Here, A and P are respectively the area and perimeter of the cross section. For all three shapes, the relationship between $\tilde{g}$ and G is numerically determined. Patzek [44] and Oren et al [42] have built

single phase network flow models that include all three shapes and approximate the $\tilde{g}$ and G relationship by

$$\tilde{g}_T = 0.6G, \text{ when } G \leq \sqrt{3}/36 \quad (22)$$

$$\tilde{g}_S = 0.5623G, \text{ when } \sqrt{3}/36 \leq G \leq 1/16 \quad (23)$$

$$\tilde{g}_C = 0.5G, \text{ when } 1/16 \leq G \leq 1/4\pi \quad (24)$$

where T stands for triangle shaped, S stands for square shaped and C stands for circular cross sections. Applied to our data, the throat shape factor can be computed by using the exact geometry of each throat.

This shape factor model assumes that a throat channel is a capillary tube having constant cross-sections. However, the linear approximation of the $\tilde{g}$ ((22)-(24))usually overestimates the fluid conductance for small shape factors and underestimates fluid conductance for large shape factors [57].

4.3.2 Lattice-Boltzman computation of hydraulic conductance

One of the advantages of LB computation is that it can capture the real geometric characteristics of channel connections rather than assuming a cylinder of constant cross-section of shape.

3DMA-Rock implements both the three-dimensional Bhatnagar-Gross-Krook (BGK) model and multiple-relaxation-time (MRT) models, with 19 velocities allowed at each site (D3Q19) to calculate the conductance for each single throat. D3Q19 is more computationally stable than D3Q15 (15 velocities) and more time efficient than D3Q27 (27 velocities). The BGK model is popular due to its simplicity, although the MRT models have been developed for improved stability.

Given measured channel geometries in the vicinity of each throat, either

type of LB model can be used to compute channel conductances. We utilized the BGK model, which is briefly summarized below.

Let $f_i(\vec{x},t)$ denote the probability that lattice location $\vec{x}$ has the velocity $\vec{e_i}$, $i = 0, ..., 18$, where the digitized velocities (see Fig. 14) are

$$e_i = \begin{cases} (0,0,0), & \text{i=0; (at rest);} \\ (\pm 1,0,0),(0,\pm 1,0),(0,0,\pm 1) & \text{i=1,...6;} \\ (\pm 1,\pm 1,0),(\pm 1,0,\pm 1),(0,\pm 1,\pm 1) & \text{i=7,...18.} \end{cases}$$

The density of the fluid $\rho = \Sigma_i f_i$ and the momentum is $\rho\vec{u} = \Sigma_i f_i \vec{e_i}$. The evolution of the distribution function f_i is described by

$$f_i(\vec{x}+\vec{e_i}\Delta t, t+\Delta t) = f_i(\vec{x},t) + \frac{1}{\tau}[f_i^{eq}(\rho(\vec{x},t),\vec{u}(\vec{x},\rho,t)) - f_i(\vec{x},t)] - 3\frac{w_i}{c^2}\Delta t\vec{e_i}\cdot\nabla p, \tag{25}$$

which consists of a collision step proportional to $\frac{1}{\tau}$ and a translation step under a pressure gradient ∇p. The equilibrium distribution function, f_i^{eq} is

$$f_i^{eq} = \rho w_i[1 + \frac{3}{c^2}\vec{e_i}\cdot\vec{u} + \frac{9}{c^4}(\vec{e_i}\cdot\vec{u})^2 - \frac{3}{2c^2}\vec{u}\cdot\vec{u}]. \tag{26}$$

The weights w_i's are defined as

$$w_i = \begin{cases} \frac{1}{3}, & \text{i=0;} \\ \frac{1}{18}, & \text{i=1,...6;} \\ \frac{1}{36}, & \text{i=7,...18.} \end{cases}$$

During a collision step, each distribution function is updated toward the equilibrium distribution, f_i^{eq}, at the rate of $1/\tau$, where τ is the single relaxation parameter and is chosen to produce the kinetic fluid viscosity $\nu = \frac{2\tau-1}{6}c^2\Delta t$. To achieve convergence, τ must be in the range $[0.525, 1.2]$ [49]. The time increment Δt is determined from the relation $c = \frac{\Delta x}{\Delta t}$ where Δx is the digitized inter-lattice site length and $c = c_s\sqrt{3}$ is the lattice speed, related to the sound

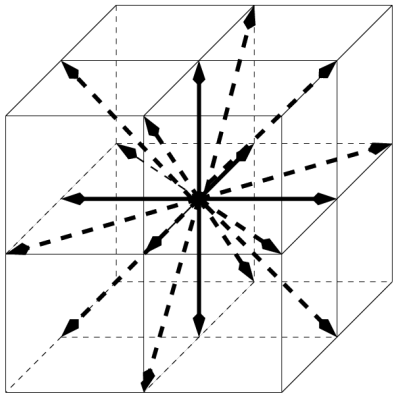

Figure 14: Discrete velocity direction of D3Q19. Solid line vectors are the velocities connecting to the nearest neighbors (of length 1 in lattice units), and dashed vectors are the velocities to the second-nearest neighbors (of length $\sqrt{2}$).

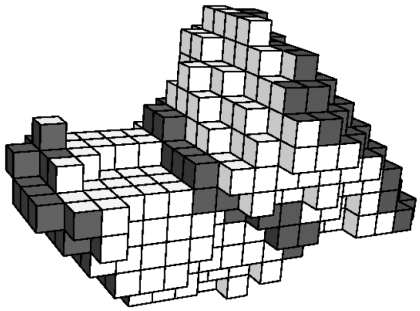

Figure 15: A digitized pore space within a distance of 6 voxels on each side. Inlet, outlet and throat barrier are in dark grey

speed for the fluid being transported, in this case, water having $c_s = 1482$ m/s.

It is necessary to define the throat computation domain for the purpose of computing conductance. 3DMA-Rock identifies the channel of the pore space as far as 6 voxels on each side of a throat barrier (the set of connected

voxels that constitutes the throat cross area). This region was computed by a 6-connected grassfire algorithm. (See Fig. 15)

Since we are interested in the channel conductance at steady state flow conditions, we set the stopping criterion for the time stepping based upon maximum difference of relative velocities at each node,

$$\frac{\|\vec{u}(x,t+\Delta t)-\vec{u}(x,t)\|_2}{\|\vec{u}(x,t)\|_2} < \epsilon. \tag{27}$$

In the calculations, we used a tolerance value of $\epsilon = 10^{-6}$.

The BGK algorithm in 3DMA-Rock uses a curved boundary scheme ([58, 66]) for no-slip boundary conditions, which provides improved convergence to steady state flow conditions comparing to standard bounce-back boundary conditions.

For inlet/outlet boundary conditions, we required $\partial\vec{u}/\partial\hat{n} = 0$, where $\hat{n}$ denotes the unit vector in the direction of the pressure gradient. In our network model, this unit vector follows the direction of the medial axis. Implementation of this boundary condition is then obtained by copying values of appropriate f_i across the boundary. Since neither inlet nor outlet surface is planar, it is not always possible to find an appropriate neighbor to copy values from, and those nodes are temporarily left at equilibrium values.

4.3.3 LB computation based power law model

The BGK computation for conductances which capture the complex shape in the vicinity of each throat, yielding a more accurate computation of fluid conductance. However, the success rate of completing a computation for a throat is lower when the sample porosity is higher. There are two main reasons for the failures. One is that BGK computation returns a negative conductance (for about 5 % of the channels computed in the Hanford column sample), when

the net flow computed opposes the direction of the pressure gradient. Upon investigation, this appears due to the pressure of computed circulation currents resulting from geometrical complexity of the channel in relation to imposed input/output boundaries. The second reason is that the BGK computation doesn't achieve velocity convergence in the throat computation domain ($\sim$10% of the channels in the Hanford column sample). Both of these these two failure rates increase with the increase in sample porosity. With the larger porosity, comes greater complex of the geometry structure of the pore space as well as more (large) pores with high coordination number.

Table 8 lists the number of throats whose conductance was successfully obtained by the BGK calculation for both C1 and C2 sections. The successful rate of the BGK computation dropped drastically from 86.3% to 64.4% when the porosity of the sample increased by only 4% (from 31% to 35%). Note that in [56], the analysis on the Fontainebleau data, whose pore space is more homogeneous and porosity is usually much smaller (ranges from 7.5% to 22%), the conductance of more than 80% of throats were successfully obtained by the BGK computation.

To correct for failures, we used a LB calculation corrected shape factor method introduced by Sholokhova [56] to provide an effective conductance for each throat channel. In [56], a single phase conductance through each throat region identified by 3DMA-Rock was computed via the BGK method, as described in Section 4.3.2. Least square fits of the form $\tilde{g} = \tilde{g}_1 G^p$ were found using the results from the successful BGK calculations. The dimensionless conductance of the throats where the LB calculation failed was then approximated using the fit.

The LB calculation corrected shape factor method performs more accurate in predicting the hydraulic conductance for Fontainebleau images [56]. Here we applied this method on the Hanford sediment samples.

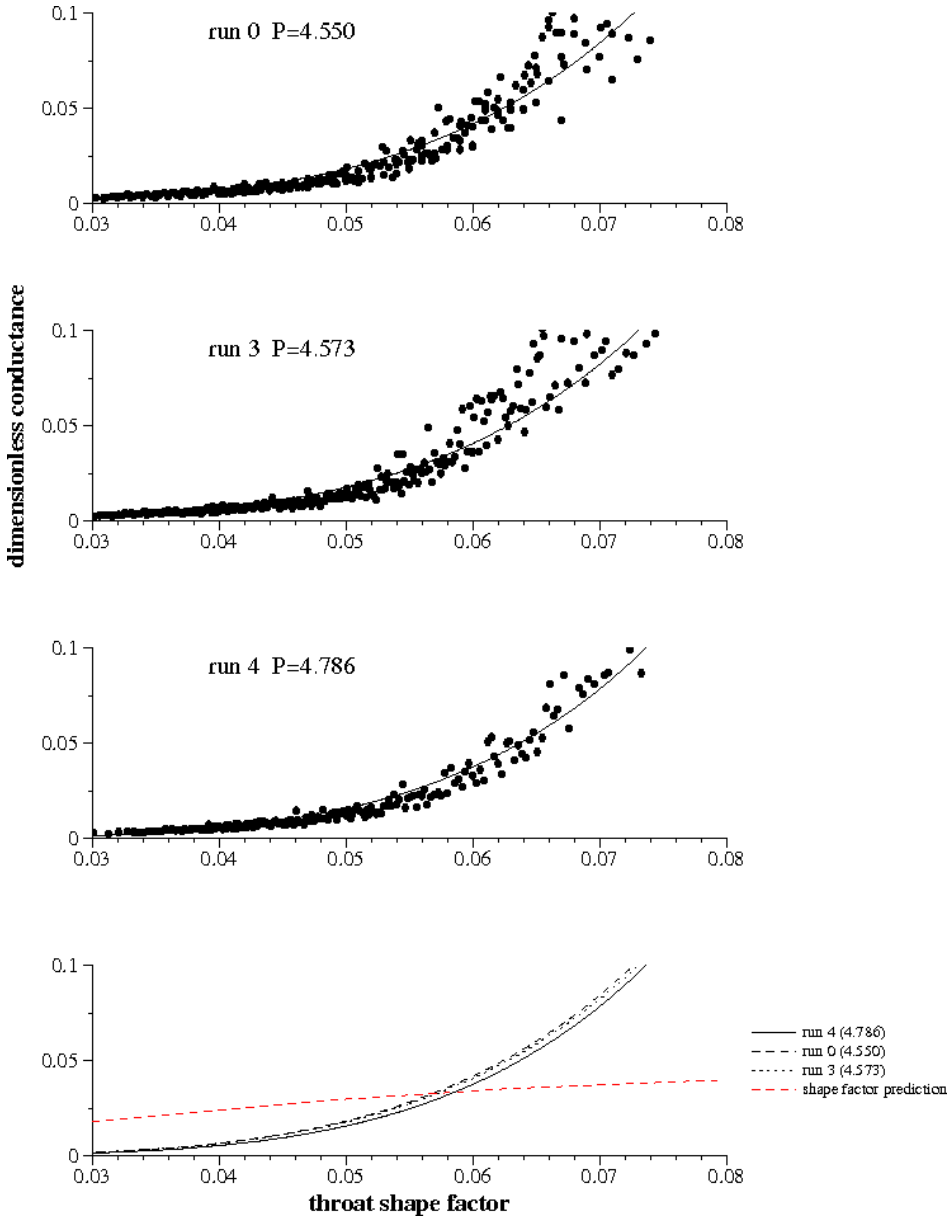

Figure 16: Top three plots: Least-square fit of the form $\tilde{g}\ G^p$ (solid curve) to the median values (circles) of the LB-computed dimensionless conductance of run 0, 3, 4 including the throats from both C1 and C2 sections. Bottom plot: comparison of power fit curve with prediction based upon the shape factor model for the Hanford sediment column throughout the time (black curve).

Day	Porosity	# Throats in the network	# Throats with g found by LB(%)
0	35%	46305	29819 (64.4%)
86	33%	40495	29400 (72.6%)
106	31%	22052	19030 (86.3%)

Table 8: BGK-computation successful rate (both C1 and C2 sections) in finding the throat conductance for the Hanford sediment sample at different days. The successful rate is higher when the porosity of the sample is smaller.

For each sample, Fig. 16 summarizes the median value of LB-computed dimensionless conductance as a function of the throat shape factor. Our LB-computation based power-law fit with p values of approximately 4.5 to 4.8 provide a more accurate prediction of the throat conductivity compared with the traditional shape factor model.

4.4 Activity Coefficients Computation

For each chemical ions in the solution, the concentration ($[\cdot]$) is related to its activity $\cdot$ by a coefficient (activity coefficient, γ).

$$[\cdot] = \gamma\{\cdot\} \tag{28}$$

The γ value varies by species, solution and temperature. However, it is possible to quantitatively predict this value for dilute solutions. One of the most important factor that determine the activity coefficient is the ionic strength (I) of the solution, which is given by the well-known formula:

$$I = \frac{1}{2}\sum_i m_i \mathrm{Z}_i^2 \tag{29}$$

, where the subscript i stands for each ion in the solution, Z_i is the charge for ion i, m_i is the molar weight for ion i.

There are several different ways to calculate the activity coefficient.

1. Debye-Huckel Limiting Law

$$\log\gamma_i = -AZ_i^2\sqrt{I}, \tag{30}$$

where $A = 1.82 \times 10^6(\sigma T)^{-3/2}$ and σ is the dielectric constant. At $25°C$, $A = 0.51$.

This law only works for the conditions which are "almost" infinite dilute ($I < 0.01$). It is assumed that ions were so far apart that the sizes of the solvated ions were ignorable. It is of very limited usage.

2. Extended Debye-Huckel Law

$$\log\gamma_i = -\frac{AZ_i^2\sqrt{I}}{1 + (\alpha_i\sqrt{\mu}/305)} \tag{31}$$

, where α_i is the size parameter for each ion. The extended Debye-Huckel Law attempts to account for ion size (α) effects, and can be used to estimate the activity coefficients for ions in the solution with $0.01 \leq I \leq 0.1$.

However, both above Debye-Huckel laws provide bad estimates for the activity coefficients when the solution has higher ionic strength ($I > 0.1$).

A third equation, Davies equation works better for the solution with high ionic strength.

3. Davies Equation

$$\log\gamma_i = Z_i^2(\frac{-A\sqrt{\mu}}{1.0 + \sqrt{\mu}} - 0.2\mu) \tag{32}$$

The advantage of the Davies equation is its better empirical description of ionic effects at higher concentrations, although its "generic" form which will not represent size effects as accurately as the extended law and other methods.

There is another popular equation, the Pitzer equation [46], for the solution

of high ionic strength. However, the Pitzer equation requires more parameters that can only be derived from experiment for every specific reaction. A database of the parameters has not been found to completely cover the chemical species and reactions in our problem. The implementation also involves much complicated computation, which is not applicable in our network model at the current stage.

In this work, the ionic strength is high (> 1) due to the high concentration of the species. We used Davies equation to compute the activity coefficients for the equilibrium computation.

4.5 Results and Discussion

The simulation performed a 6-hour flow-column and 6-hour batch experiment sequence, mimicking the two major flow regimes to which the Hanford soil column was subjected.

4.5.1 Flow-column experiment simulation

1. pH Value and Dissolution

The local pH value of the solution is the leading control on the dissolution rate. Fig. 17 shows the development of the average pH with time. Average pH increases rapidly initially, reaching a maximum of 12.78 after 15 minutes of flow. Subsequently, the pH value dropped, first slowly and then more rapidly, reaching an effective steady state value of 11.88 after 1.8 hours of flow. The initial rise in pH is due to the injected solution moving through. This rapid rise in pH drives SiO_2 dissolution. The subsequent reduction in pH is explained by the SiO_2 dissolution which consumes OH^- and produces free H^+.

With concentration increases of aqueous silica and aluminum, the reactive fluid inside the column becomes supersaturated, and the nitrate-cancrinite

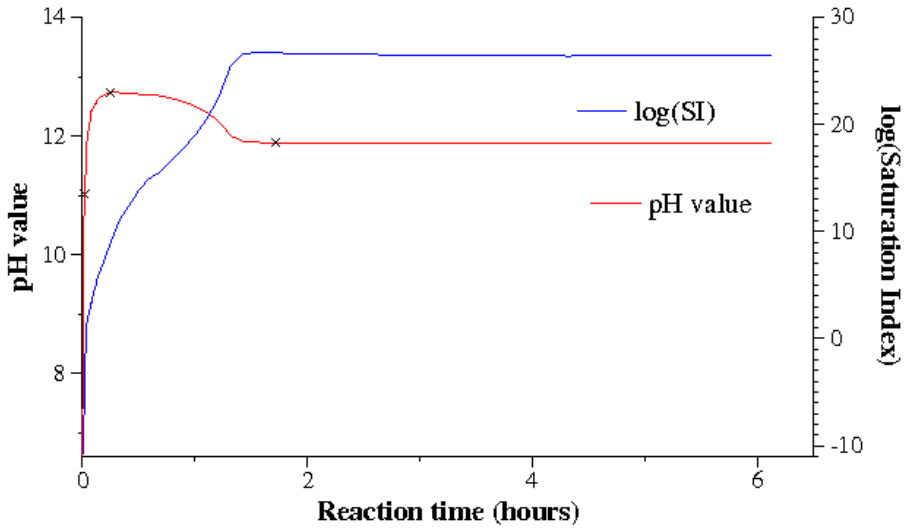

Figure 17: The evolution of pH value (red curve) and saturation index (green curve) of the fluid inside the column during the flow-column experiment simulation. The points that represent the pH value at reaction time 1 minute (initial increase), 15 minutes (reaching maximum), and 1.8 hours (stabilized) are marked on the curve.

starts to precipitate, releasing additional OH^- anions into the solution. Our observation of drop in the pH value indicates that after 15 minutes of reactive fluid injection, the rate of OH^- release by precipitation was slower than the removal rate of OH^- by dissolution, and by 1.5 hours the release/removal rate stabilizes.

2. Saturation Index (SI) and Precipitation

Precipitation begins when the saturation index (Ω) exceeds 1 ($\log\Omega > 0$). This occurred less than 1 minute after the reactive flow. The increasing value of Ω indicates that more and more pores started to precipitate; all the pores were observed to precipitate after around 0.5 hours.

3. [Si], [Al] Evolution throughtout the Time

Fig. 18 plots the average concentrations inside the column as well as the effluent concentrations of Si and Al ions. As the Al ions only come from the

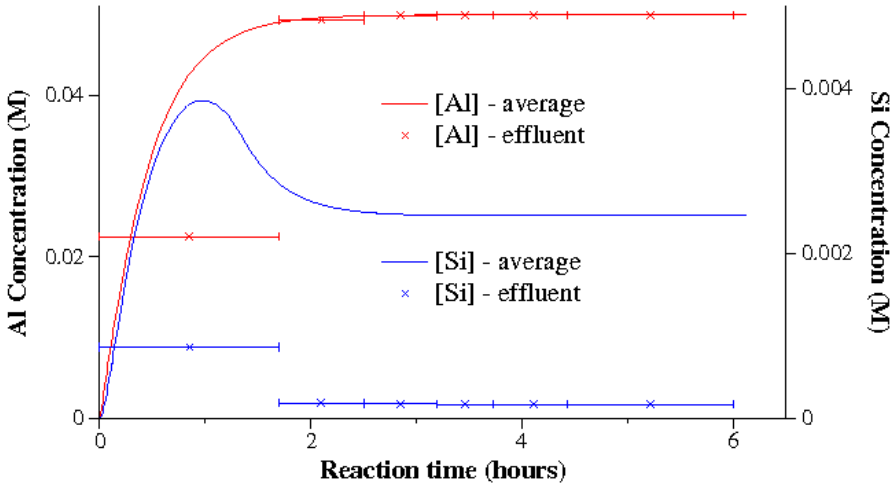

Figure 18: The concentration evolution of Si (blue curve), and Al (red curve) ions inside the column during the flow-column experiment simulation. The average concentrations of Si experienced an increase at the beginning and a reduction period after 1 hour exposure time to the reactive fluid. The average concentration of Al increased monotonically to the concentration of the flow-in solution. The average effluent concentrations of Si (red horizontal bar) and Al.(blue horizontal bar) were computed over time-scaled equivalent periods as the effluent measurements in the experiment. The horizontal bars shows both the time period for each equivalent effluent accumulation and the averaged concentrations.

injected solution, the increase of the average aluminum reflected this species advection process. After two hours of flow, the average concentration of aluminum ions reached 0.495 M; after 6 hours, it was 0.498 M (approaching the 0.05 M concentration for the injected solution).

After the high alkaline solution contacted the quartz grains, quartz was dissolved and silicic acid was released into the solution. This increase in the silica ion concentration reached a peak of 0.0039 M after one hour and started to drop as a result of secondary precipitation. With the increase of Si ion concentration, the solution in the column became super-saturated, and started

to precipitate cancrinite. The precipitation rate was controlled by the concentration of both Si and Al in the fluid, yet dominated by the Al species. As the concentration of aluminum ions became larger and larger, more and more silicic acid was consumed by this precipitation. Consequently, when the dissolution rate of Si ions failed to catch up the consumption rate during the precipitation, decrease of Si concentration occurred. The aluminum ion concentration was not significantly affected, since the Al concentration in the injected solution was sufficient to make up for the loss of aluminum ions in precipitation.

The drop in Si concentration was stabilized after 2 hours reaction. This stabilization of Si concentration matched with the stabilization of pH value and saturation index of the fluid in the column, indicating equilibrium between dissolution and precipitation.

The effluent concentrations of Si and Al ions over various period of time were also tracked in the simulation. Notice that our simulation domain is 2.4 mm long, covering a short section of the 8.8 cm long column in the Hanford flow-column experiment. This has the effect that under the same average flow velocity, it takes longer for the injected fluid to flow through the whole column in the experiment than in the simulation. Thus, in order to compare the effluent concentration trends with the experiment measurement, we need to scale the time length of the experiment. We estimate the scaling factor as the ratio, 0.0273, of the computational length to the experimental column domain length. Fig. 18 plots effluent concentrations of Si and Al ions averaged over the time-scaled equivalent periods to match the first six effluent measurements in the experiment. Our simulated effluent concentration of Si ion shows an initial increase to 8.67×10^{-4} M after 1.7 hours (equivalent to 62.5 hours in the experiment) and a following drop to 1.903×10^{-4} M after 2.5 hours (equivalent to 110 hours in the experiment) and stabilization to 1.7×10^{-4} M after

3 hours (equivalent to 133 hours in the experiment). The simulated effluent concentration change of Si was qualitatively consistent with the the experiment measurement. However, our effluent concentration of Al ions didn't show the reduction after 2.5 hours as measured in the experiment. We also noticed that, compared with the experiment, we obtained much smaller Si effluent concentration and much larger Al effluent concentration. This can be explained by the volume of our simulation domain. Considering that the effluent concentrations measured in the experiments are the accumulative amount of ions divided by the total volume of out flow from the outlet of the column, the collected Si ions included the dissolved silicic acid from the whole column, while our simulation, only captured Si ions that were dissolved from the grain surface in the subcolumn, the smaller Si effluent concentration is understandable. Meanwhile, with the same volume of fluid injected, the whole column consumed more Al ions than the subcolumn in the simulation, resulting in a smaller Al effluent concentration measured in the experiment.

4.5.2 Batch experiment simulation

After six hours of flow-column experiment, we observed the stabilization of both pH value and saturation index of the fluid inside the column. With these two values unchanged, the precipitation and dissolution rate also stabilized. Thus, we stopped the in-flow solution and started to simulate the concentration changes of Si and Al under batch experiments condition.

Under the batch experiment simulation, only diffusion of the chemical species and chemical reactions took place in the column. Since there was no more injected solution, Na^+, NO_3^{-1}, and Al^{3+} ions were no longer replenished when consumed by precipitation process. Meanwhile, dissolution kept releasing Si ions into the solution under the high alkaline environment. Precipitation continued, at a slow rate as the concentration of Al ions decreased.

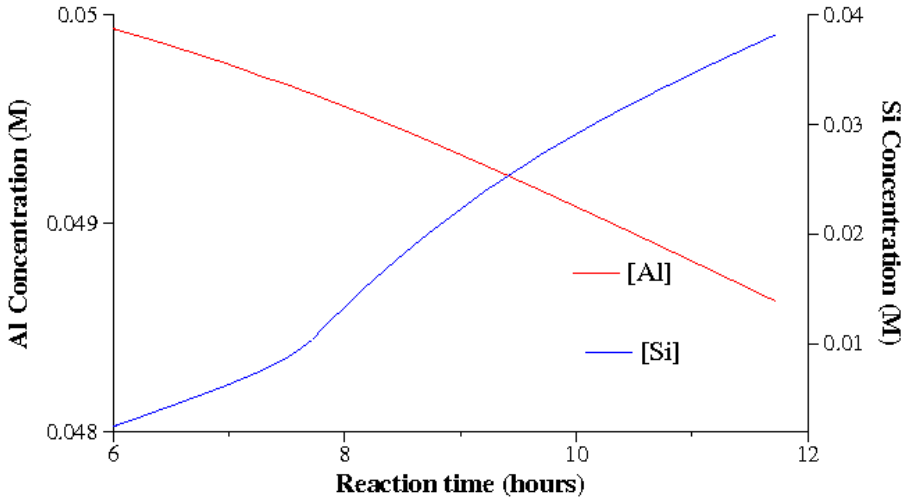

Figure 19: The concentration evolution of Si (green curve), and Al (red curve) ions inside the column during the batch experiment simulation. The simulation started at the end of 6-hour flow-column simulation. The Si concentration (green curve) experienced a monotonic increase due to the dissolution. The average Al concentration decreased monotonically, which was consumed in the secondary precipitation.

Decreasing precipitation means decreasing uptake of silicic acid. As a consequence, we observed a bounce back in the concentration of Si in the fluid. The corresponding pH value also increased.

The evolution of Si and Al concentration during this batch simulation period is shown in Fig. 19. After 6-hour of reactions without in-flow, the average concentration of Al was reduced by 4%, whereas the average concentration of Si was almost 10 times larger than at the beginning of this batch reaction period.

The increase in the Si concentration is qualitatively consistent with the effluent concentration of Si measured at the beginning of Run 2. Notice that the column in the experiment also performed as a batch reactor when it was sealed and shipped for imaging, a high Si concentration was observed at the

beginning of next run (see Fig. 10), indicating that dissolution again dominated during the shut-in period.

As was mentioned in Section 4.2, the reduction in pore surface area available for dissolution is not considered in the current version of the reactive model. Under this restriction, we expect to see the Si concentration increase linearly while the Al concentration should monotonically decrease to zero. Therefore, we stopped the batch experiment simulation after a 6 hour reaction period.

Chapter 5

Discussion and Summary

We have shown the capacity of X-ray computed micro-tomography to capture and quantify snapshots in time of dissolution and secondary precipitation in the microstructure of Hanford sediments exposed to simulated caustic waste in flow-column experiments. Analysis of the image indicates that dissolution processes dominated in the larger pores while precipitation filled in small pores and clogged small throats. In addition to the expected loss of pore-to-pore connectivity accompanying throat clogging, there is a drastic loss in network connectivity, although without a significant increase in geometric tortuosity of the remaining pathways.

The reactive network flow model developed in this work is a preliminary study. The numerical simulation of the flow column experiment (run 1) captured the initial short-time dominance of SiO_2 dissolution followed by build up, and later dominance of, cancrinite precipitation. The simulated effluent concentrations were compared with the experiment measurements with reaction time approximately scaled to the computation domain. The simulation results showed qualitative consistency with the experiment until reaching steady state after 2 hours of simulation reaction. However, unlike the late time values of the run 1 experiment which seem to indicate an eventual build up of SiO_2

dissolution, the numerical simulation remains in steady state.

A batch experiment was also simulated to model the column shut-in period. The rebound in Si concentration, indicating the redominance of dissolution, qualitatively matches with the experiment measurement at the beginning of run 2.

However, the model is still in its early development, the following several factors have not been considered in the simulation, which need to be addressed in future work.

1. In the flow-column reactive simulation, we failed to show to concentration rebound of Si and reduction of Al which were measured in the flow-column experiment over the period of last 29 days of run 1. Further investigation is need for the kinetics of dissolution and precipitation reactions.

2. We need to incorporate the change of the reactive area available for dissolution. When nitration cancrinite precipitates on grain surfaces, the surface area of quartz available for dissolution is reduced. This has the effect on both reduction of further dissolution and precipitation. However, in order to take this change of area into consideration, we need to further investigate the morphology of the cancrinite precipitant.

3. We need an improved method to calculate the activity coefficients for the concentrated aqueous solutions. In this work, the Davis equation was used to compute the activity coefficients. The Davis equation is simple to implement and computationally efficient, but is not accurate when the ionic strength is large. In the work of [43, 68], Pitzer's model has been employed to predict activity coefficients when the ionic strength of the aqueous solution is larger than 1 M. [68] has shown that Pitzer's model provides a better estimation of activity coefficient to experimental data. The employment of Pitzer model, which requires the computation for the interactions among all the species, will add a lot of complexity in the computation. Parallel computation should be

incorporated with implementation of the Pitzer model, since the equilibrium computation only involves in each pore can be done in parallel.

4. We need to incorporate the change of throat area and pore volume based on more quantitative results of the preferential area of dissolution and precipitation. In this work, we assumed that the throat channel remained the same all the time. However, as we have discovered in Chapter 3, dissolution and precipitation changed the throat area distribution. These changes will produce corresponding changes in channel conductance and advection of the flow in the model.

Bibliography

[1] E. Aharonov, D. Rothman. Growth of correlated pore-scale structures in sedimentary rocks. J Geophys Res 1996;101:2973-87.

[2] Y. Arai, M.A. Marcus, N. Tamura, J.A. Davis, J.M. Zachara. Spectroscopic evidence for uranium bearing precipitates in vadose zone sediments at the Hanford 300 Area site. Environ Sci Technol 2007;41:4633-9.

[3] M. C. Barnes, J. Addai-Mensah, A. R. Gerson. The mechanism of the sodalite-to-cancrinite phase transformation in synthetic spent Bayer liquor. Microporous Mesoporous Mater 1999;31:287-302.

[4] M. M. Benjamin. Water Chemistry. McGraw-Hill Series in Water Resources and Environmental Engineering. 2002: McGraw.

[5] S. Bekri, J. F. Thovert, P. M. Adler. Dissolution of Porous Media. Chem.Eng.Sci. 1995;50:2765-91.

[6] S. Bekri, J. F. Thovert, P. M. Adler. Dissolution and deposition in fractures. Eng Geol 1997;48:283-308.

[7] B. Bickmore, K. Nagy, J. Young, J. Drexler. Nitrate-cancrinite precipitation on quartz sand in simulated Hanford tank solutions. Environ Sci Technol 2001;35:4481-6.

[8] R. Cai, W. B. Lindquist, W. Un, K. W. Jones. Tomographic analysis of reactive flow induced pore sturcture changes in column experiments. Adv Water Resour 2009;32:1396:403

[9] S. Choi, P. A. O'Day, N. A. Rivera, K. T. Mueller, M. Vairavamurthy, S. Seraphin, J. Chorover. Strontium speciation during reaction of kaolinite with simulated tank-waste leachate: Bulk and microfocused EXAFS analysis. Environ Sci Technol 2006;40:2608-14.

[10] J. Chorover, S. Choi, M. Amistadi, K. Karthikeyan, G. Crosson, K. Mueller. Linking cesium and strontium uptake to kaolinite weathering in simulated tank waste leachate. Environ Sci Technol 2003;37:2200-08.

[11] G. Daccord, O. Lietard, R. Lenormand. Chemical dissolution of a porous-medium by a reactive fluid: 2. Convection vs reaction, behavior diagram. Chem Eng Sci 1993;48:179-86.

[12] G. Daccord. Chemical dissolution of a porous-medium by a reactive fluid. Phys Review Lett 1987;58:479-82.

[13] K. L. Damico, J. H. Dunsmuir, S. R. Ferguson, B. P. Flannery, H. W. Deckman. The Exxon microtomography beam line at the National Synchrotron Light Source. Rev Sci Instrum 1992;63:574-7.

[14] Y. Deng, M. Flury, J. B. Harsha, A. R. Felmy and O. Qafoku. Cancrinite and sodalite formation in the presence of cesium, potassium, magnesium, calcium and strontium in Hanford tank waste simulants. Applied Geochem 2006;21:2049-63.

[15] Y. Deng, J. B. Harsha, M. Flury, J. S. Young, J. S. Boyle. Mineral formation during simulated leaks of Hanford waste tanks. Applied Geochem 2006;21:1392-409.

[16] R. L. Detwiler, R. J. Glass, W. L. Bourcier. Experimental observations of fracture dissolution: The role of Peclet number on evolving aperture variability. Geophys Res Lett 2003;30:4.

[17] P. E. Dijk, B. Berkowitz, Y. Yechieli. Measurement and analysis of dissolution patterns in rock fractures. Water Resour Res 2002;38:12.

[18] P. Dijk, B. Berkowitz. Precipitation and dissolution of reactive solutes in fractures. Water Resour Res 1998;34:457-70.

[19] W. B. Durham, W. L. Bourcier, E. A. Burton. Direct observation of reactive flow in a single fracture. Water Resour Res 2001;37:1-12.

[20] B. P. Flannery, H. W. Deckman, W. G. Roberge, K. L. Damico. 3-dimensional X-ray microtomography. Science 1987;237:1439-44.

[21] C. N. Fredd, H. S. Fogler. Influence of transport and reaction on wormhole formation in porous media. Aiche Journal 1998;44:1933-49.

[22] V. L. Freedman, D. H. Bacon, K. P. Saripalli, P. D. Meyer. A film depositional model of permeability for mineral reactions in unsaturated media. Vadose Zone J 2004;3:1414-24.

[23] M. L. Hoefner, H. S. Fogler. Pore evolution and channel formation during flow and reaction in porous-media. Aiche Journal 1998;34:45-54.

[24] W. A. House, D. R. Orr. Investigation of the pH dependence of the kinetics of quartz dissolution at 25 °C. J Chem Soc, Faraday Trans 1992;88:233-41.

[25] Q. L. Kang, P. C. Lichtner, D. X. Zhang. Lattice Boltzmann pore-scale model for multicomponent reactive transport in porous media. J Geophys Res 2006;111:B05203.

[26] Q. J. Kang, D. X. Zhang, S. Y. Chen. Simulation of dissolution and precipitation in porous media. J Geophys Res-Solid Earth 2003;108:2505

[27] T. C. Lee, R. L. Kashyap, C. N. Chu. Building skeleton models via 3-D medial surface/axis thinning algorithms. CVGIP: Graph Models Image Proc 1994;56:462-78.

[28] L. Li, C. A. Peters, M. A. Celia, Upscaling geochemical reaction rates using pore-scale network modeling. Adv Water Resour 2006;29:1357-70.

[29] P. C. Lichtner, Q. Kang. Upscaling pore-scale reactive transport equations using a multiscale continuum formulation. Water Resour Res 2007;43:19.

[30] K. Mashal, J. B. Harsh, M. Flury, A. R. Flemy. Analysis of precipitates from reaction of hyperkaline solutons with soluble silica. Appl Geochem 2005;20:1357-67.

[31] W. B. Lindquist. 3DMA-Rock: A software package for automated analysis of rock pore structure in 3-D computed microtography images. URL: http://www.ams.sunysb.edu/ lindquis/3dma/3dma_rock/3dma_rock.html

[32] W. B. Lindquist. 3DMA-Rock General Users Manual, Department of Applied Mathematics and Statistics State University of New York at Stony Brook, 1999.

[33] W. B. Lindquist, A. Venkatarangan, J. Dunsmuir, T. f. Wong. Pore and throat size distributions measured from sychrotron X-ray tomographic images of Fontainebleau sandstones. J Geophys Res 2005;105:21508-28.

[34] W. B. Lindquist, A. Venkatarangan. Investigating 3D geometry of porous media from high resolution images. Phys Chem Earth(A) 1999;25:593-9.

[35] W. B. Lindquist, S.-M. Lee, D. A. Coker, K. W. Jones, P. Spanne. Medial axis analysis of void structure in three-dimensional tomographic images of porous media. J Geophys Res 1996;101:8297-310.

[36] J. E. Mackin, R. C. Aller. The infinite dilution diffusion coefficient for $Al(OH)_4^-$ at 25°C. Geochim Cosmochim Acta 1983;47:959-61.

[37] G. Mason, N. R. Morrow. Capillary behavior of a perfectly wetting liquid in irregular triangular tubes. J. Colloid Interface Sci 1991;141:262-74

[38] K. Mashal, J. B. Harsh, M. Flury, A. R. Felmy, H. Zhao. Colloid Formation in Hanford Sediments Reacted with Simulated Tank Waste. Environ. Sci. Technol 2004;38(21):57506.

[39] J. P. McKinley, J. M. Zachara, C. Liu, S. C. Heald, B. I. Prenitzer, B. W. Kempshall. Microscale controls on the fate of contaminant uranium in the vadose zone, Hanford Site, Washington. Geochim Cosmochim Acta 2006;70:1873-87.

[40] M. Nyman, J. L. Krumhansl, P. Zhang, H. Anderson, T. M. Nenoff. Chemical Evolution of Leaked High-Level Liquid Wastes in Hanford Soils. Mater. Res. Soc. Symp. Proc 2000;608:225-30.

[41] W. Oh, W. B. Lindquist. Image thresholding by indicator kriging. IEEE Trans Pattern Anal Mach Intell 1999;21:590-602.

[42] P.-E Oren, S. Bakke, O. J. Arntzen. Extending Predictive Capabilities to Network Models. SPE J. 1998;3:324-35

[43] H. Park, P. Englezos. Osmotic coefficient data for NaOH-NaCL-NaAl(OH)4-H2O system measured by an isopiestic method and modeled using Pitzer's model at 298.15K. Fluid Phase equilibria. 1999;155:251-9

[44] T. W. Patzek. Verification of a Complete Pore Network Model of Drainage and Imbibition. SPE J. 2001;6:144-56

[45] T. W. Patzek, D. B. Silin. Shape Factor and Hydraulic Conductance in Noncircular Capillaries: I. One-Phase Creeping Flow. J. Colloid Interface Sci 2001;236:295-304.

[46] K. S. Ptizer, G. Mayorga. Thermodynamics of electrolytes. II. Activity and osmotic coefficients for strong electrolytes with one or both ions univalent. J. Phys. Chem 1973.77:2300-7.

[47] M. Prodanovic, W. B. Lindquist, R. S. Seright. Porous structure and fluid partitioning in polyethylene cores from 3D X-ray microtomographic imaging. J Colloid Interf Sci 2006;298:282-97.

[48] M. Prodanovic, W. B. Lindquist, R. S. Seright. 3D image-based characterization of fluid displacement in a Berea core. Adv Water Resour 2006;30:214-26.

[49] M. Prodanovic, W. B. Lindquist, R. S. Seright. 3D image-based characterization of fluid displacement in a Berea core. Adv. Water Resour 2007;30:214-26.

[50] N. P. Qafoku, C. C. Ainsworth, J. E. Szecsody, O. S. Qafoku. Aluminum effect on dissolution and precipitation under hyperkaline conditions: I. Liquid phase transformation. J Environ Qual 2003;32:2354-63.

[51] N. P. Qafoku, C. C. Ainsworth, J. E. Szecsody, D. L. Bish, J. S. Young, D. E. McCready, O. S. Qafoku. Aluminum effect on dissolution and precipitation under hyperkaline conditions: II. Solid phase transformations. J Environ Qual 2003;32:2364-72.

[52] N. P. Qafoku, C. C. Ainsworth, J. E. Szecsody, O. S. Qafoku. Transport-controlled kinetics of dissolution and precipitation in the sediments under alkaline and saline conditions . Geochim Cosmochim Acta 2004;68(14):2981-95.

[53] M. L. Rivers, S. R. Sutton, P. J. Eng, Geoscience pplications of X-ray computed microtomography. Developments in X-Ray Tomography II 1999;3772:78-86. http://cars9.uchicago.edu/software/tomography.html

[54] R. J. Serne, B. N. Bjornstad, D. G. Horton, D. C. Lanigan, C. W. Lindenmeier, M. J. Lindberg, R. E. Clayton, V. L. LeGore, R. D. Orr, I. V. Kutnyakov, S. R. Baum, K. N. Geiszler, M. M. Valenta, T. S. Vickerman, H. T. Schaef. Characterization of vadose zone sediments below the T Tank Farm: Boreholes C4104, C4105, 299-W10-196 and RCRA Borehole 299-W11-39. Tech Rep PNNL-14849, Pacific Northwest National Laboratory 2004.

[55] H. Shin, W. B. Lindquist, D. L. Sahagian, S. R. Song. Analysis of the vesicular structure of basalts. Comput Geosci 2005;31:473-87.

[56] Y. Sholokhova, D. Kim, W. B. Lindquist. Network flow modeling via lattice-Boltzmann based channel conductance. Adv Water Resour 2008;doi:10.1016/j.advwatres.2008.10.016

[57] Y. Sholokhova. Network Flow Modeling via Lattice-Boltzmann Based Channel Conductance. Prediction of Relative Permeability in Primary Drainage. PhD thesis, 2009.

[58] W. Shyy, R. Mei, L.S. luo. An accurate curved boundary treatment in the lattice boltzmann method. J Computational Phys, 1999;155:307-30.

[59] P. Szymczak, A. J. C. Ladd. A network model of channel competition in fracture dissolution. Geophys Res Lett 2006;33:4.

[60] P. Szymczak, A. J. C. Ladd. Microscopic simulations of fracture dissolution. Geophys Res Lett 2004;31:4.

[61] E. Tentheroy, C. Scholz, E. Aharonov, A. Leger. Precipitation sealing and digenesis: 1. Experimental results. J Geophys Res 1998;103:23,951-68.

[62] W. Um, R. J. Serne, S. B. Yabusaki, A. T. Owen. Enhanced radionuclide immobility and flow-path change by dissolution and secondary precipitates at the Hanford Site. J Environ Qual 2005;34:1404-14.

[63] W. Um, R. J. Serne, K. M. Krupka. Linearity and Reversibility of Iodide Adsorption on Sediments from Hanford, Washington Under Water Saturated Conditions. Water Research 2004;38(8):2009-2016.

[64] W. Um, R. J. Serne. Sorption and transport behavior of radionuclides in the proposed low-level radioactive waste facility at the Hanford Site, Washington. Radiochim Acta 2005;93:57-63.

[65] W. Um, R.J. Serne, S. B. Yabusaki, A. T. Owen. Enhanced radionuclide immobility and flow-path change by dissolution and secondary precipitates at the Hanford Site. J Environ Qual 2005;34:1404-14.

[66] D. Yu, W. Shyy, R. Mei, L.S. Luo. Lattice Boltzmann method for 3d flows with curved boundary. J Computational Phys. 2000;161:689-99.

[67] Z. Wang, J. M. Zachara, P. L. Gassman, C. Liu, O. Qafoku, W. Yantasee, et al. Fluroescence spectroscopy of U(VI)-silicates and U(VI)-contaminated Hanford sediment. Geochim Cosmochim Acta 2005;69:1391-403.

[68] G. Zhang, Z. Zheng, J. Wan. Modeling reactive geochemical transport of concentrated aqueous solutions. Water Resour. Res. 2005;41:W02018

[69] B. V. Zhmud, W. A. House, F. H. Denison. Release kinetics and concentration profile of dissolved silicon in compacted sediments. J Chem Soc, Faraday Trans 1997;93:3473-8.